DTI© FILE COPY

LABORATORY OF PLASMA STUDIES

Papers by Cornell Authors to be Published in the
Proceedings of the VI International Conference
on High Power Particle Beams
Kobe, Japan June 9-12, 1986

LPS 357   June 1986

DTIC
ELECTE
APR 13 1990
E

CORNELL UNIVERSITY
ITHACA, NEW YORK

90 04 12 156

Papers by Cornell Authors to be Published in the

Proceedings of the VI International Conference

on High Power Particle Beams

Kobe, Japan   June 9-12, 1986

LPS 357   June 1986

DTIC
ELECTE
S APR 13 1990
E D

Table of Contents

ELECTRON LEAKAGE CAUSED BY STOCHASTIC ELECTRON MOTION IN MAGNETICALLY INSULATED DIODES

M. P. Desjarlais and R. N. Sudan

Laboratory of Plasma Studies
Cornell University
Ithaca, New York 14853

Abstract

The diffusion of electrons and the associated leakage current is investigated for magnetically insulated systems. The diffusion results from stochastic motion of the electrons in a weakly nonuniform electric field. The model system is planar and periodic in the electron drift direction. Leakage currents, normalized to the Child-Langmuir current, are obtained as a function of the insulation parameter B/B_c. Very good agreement with experimental results is obtained for electric field perturbations on the order of 5 to 7% of the uniform equilibrium field.

Introduction

Magnetic insulation of electrons in crossed-field devices plays a crucial role in the generation of high-power ion beams and the operation of magnetically insulated transmission lines. Successful application of these devices requires that electron losses be kept to tolerable levels. Simple models for the electron sheath that assume symmetry in the drift direction predict complete insulation for sufficiently large magnetic fields. Breaking of this symmetry, whether by imperfections of construction or the spontaneous growth of fluctuations, may result in stochastic wandering of the sheath electrons and the generation of an associated leakage current.

In an earlier work [1], we investigated the transition to stochasticity for electron motion in the field configuration of a magnetically insulated diode; action-angle variables were introduced to facilitate the nonlinear analysis and the criterion for stochasticity was established. In this paper, we calculate the resulting diffusion and leakage currents. Using quasilinear theory, the diffusion co-efficient is calculated for a diffusion equation relevant to electrons in the globally stochastic regions. The steady-state diffusion equation is solved to yield the distribution function of electrons in action space. Normalizing the distribution function to the globally stochastic fraction of the equilibrium electrons provides a leakage current. The analysis yields very good agreement with the experimental results of Orzechowski and Bekefi [2] on leakage currents in a magnetically insulated device.

Equilibria

The equilibria used in the analysis consist of a constant-density, non-relativistic electron sheath, a uniform applied magnetic field $\mathbf{B} = B_0\hat{z}$, and an applied voltage V across a planar, periodic gap of length L and width d. The equilibrium sheath is assumed to be confined on the cathode side with height x_s, where $0 \leq x_s \leq d$. The geometry is illustrated in Fig. 1. The $\hat{z}$ direction is ignored throughout the analysis. The mean flow is in the $\hat{y}$ direction.

Fig. 1.   Geometry and coordinate system.
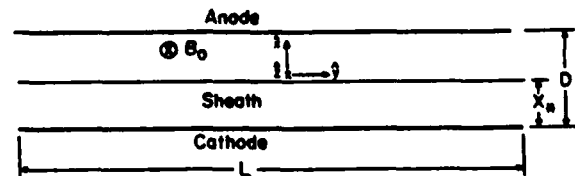
The single particle Hamiltonian for the region $0 \leq x \leq x_s$ can be written in the dimensionless form

$$H = \frac{P_x^2}{2} + \frac{(P_y + x)^2}{2} - Q\frac{x^2}{2}, \qquad (1)$$

where $Q = (2e\phi_s/m\Omega^2 x_s^2)$ and ϕ_s is the potential at the sheath surface. Distances are normalized to x_s, momenta to $m\Omega x_s$, and time to $1/\Omega$. The parameter Q

is equal to ω_p^2/Ω^2, where ω_p is the electron plasma frequency and Ω is the electron cyclotron frequency. The Hamiltonian (1) defines a class of systems parametrized by Q. The well-known Brillouin flow equilibrium [3] is obtained with $Q = 1$. Equilibria exist for the range $0 < Q \leq 1$.

The equilibrium Hamiltonian can be cast in convenient form for perturbation analysis through the use of canonical transformations. The Hamiltonian in action-angle variables [1] becomes

$$H = \omega J_\theta + \left(1 - \frac{1}{\omega^2}\right)\left(\frac{2\pi}{L}\right)^2 \frac{J_\phi^2}{2}, \qquad (2)$$

where

$$J_\theta = \frac{\omega}{2}\left[\left(x + \frac{P_y}{\omega^2}\right)^2 + \frac{P_x^2}{\omega^2}\right], \qquad (3)$$

$\omega^2 = 1 - Q$, and $J_\phi = (L/2\pi)P_y$. The two characteristic frequencies are $\omega_\theta = \omega$, which corresponds to the x-direction bounce frequency, and $\omega_\phi = (2\pi/L)^2 J_\phi(1 - \omega^{-2})$, which corresponds to the y-direction transit frequency.

Stochasticity and Diffusion

In the absence of perturbations, an electron initially confined to the sheath region may remain so indefinitely. This permits complete insulation for a sufficient magnetic field. For non-relativistic systems in which all the electrons have zero energy H and canonical momentum P_y, this critical field is given by $B_c = c(2mV/e)^{1/2}/d$ [4]. In the presence of perturbations, the situation is much more complicated. For small perturbations, local invariants, known as KAM surfaces [5-7], may persist that serve to barricade the electron motion and prevent leakage. The analysis in our previous paper was devoted primarily to establishing the conditions under which the KAM surfaces are destroyed and electron leakage becomes possible. We considered a dimensionless perturbation potential of the form

$$\tilde{\phi} = \Delta \frac{4Q}{\pi} x(1 - x)\sin(2\pi y/L), \qquad (4)$$

where Δ is an arbitrary amplitude factor and L is the wavelength of the perturbation normalized to x_s. The perturbation electric field and the background electric field are related in magnitude by $|\tilde{E}_{y\max}/E_{x_s}| = 2\Delta/L$. The use of action-angle variables allows us to write the perturbed Hamiltonian in the convenient form

$$H = H_0 + \Delta \sum_{k=-\infty}^{\infty} \tilde{H}_k(\mathbf{J})\sin(\phi - k\theta), \qquad (5)$$

where H_0 is given by Eq. (2). We refer the reader to Ref. 1 for details on the functional form of the $\tilde{H}_k$. The Hamiltonian (5) exhibits resonances at the stationary phase points of the driving term, i.e., where $\dot{\phi} - k\dot{\theta} = 0$. The frequencies are approximately given by the equilibrium Hamiltonian. In regions of phase space where the equilibrium frequencies satisfy the resonance condition, resonant islands will appear. Roughly speaking, if the islands are large enough to overlap, the motion of particles near the islands becomes very irregular. This is known as intrinsic stochasticity. The analysis in our previous paper indicated that the stochasticity is a sensitive function of Q. The level of stochasticity is depicted by the stochasticity parameter S, which represents the fraction of intervening phase space covered by adjacent resonances. An approximate criterion for stochasticity is due to Chirikov [8] and is given by $S > 1$. A rough approximation to the stochasticity parameter calculated in our previous paper is

$$S \leq \frac{8}{L}\frac{Q}{1 - Q}\left(\frac{\pi\Delta}{\sqrt{2}}\right)^{1/2}. \qquad (6)$$

The largest values of S are found on the $H = 0$ energy surface, where the relation approaches equality. Note that S diverges as $Q \to 1$: the Brillouin flow limit. The Brillouin flow equilibrium is globally stochastic for arbitrarily small perturbations.

In Ref. 1 we arrived at the following qualitative picture of diode saturation. The electron sheath diffuses towards the anode as a result of stochastic motion. The parameter Q decreases as the density profile spreads out over the gap. If the perturbation is sufficiently large, the sheath will spread to the anode ($x_s \to d$) and a leakage current will be established. The assumption that

the density profile remains relatively flat yields a simple relation between the saturated value of Q and B_c, namely, $Q_{sat} = (B_c/B)^2$. Hence, the larger the value of B/B_c, the more difficult electron leakage becomes. In the following analysis, we proceed to quantify this leakage current.

A quasilinear diffusion coefficient for the stochastically wandering electrons is obtained with the standard technique of integrating the perturbation force over the unperturbed trajectories to calculate the change in action for a given initial condition as a function of time. Averaging over the initial phases allows us to form $D(J_\theta; H)$. In the interest of brevity, we omit the analysis here; details may be found in Ref. 10. The diffusion coefficient is given by $D(J_\theta; H) = T_\theta (\Delta \kappa \bar{H}_\kappa)^2/4$, where $T_\theta = 2\pi/\omega_\theta$ and $\kappa(J_\theta) = \omega_\phi(J_\theta)/\omega_\theta$. The diffusion coefficient $D(J_\theta; H)$ is found to be a monotonically increasing function of J_θ. This implies a mean shift $C = \partial D/\partial J_\theta$ [9] as well as a spreading of the single particle distribution function. Since the perturbation we consider is time-independent, the motion of a given electron is confined to a constant energy surface. Therefore, each energy surface has its own diffusion equation.

Steady-State Diffusion

Having obtained the diffusion coefficient, we consider the diffusion equation for the stochastic electrons:

$$\frac{\partial f}{\partial t} = \frac{\partial}{\partial J_\theta} D(J_\theta; H) \frac{\partial f}{\partial J_\theta} + S(J_\theta; H), \qquad (7)$$

where $S(J_\theta; H)$ is a source term. In our system, the only source of electrons is the cathode at $(J_\theta, H) = (0,0)$. Since the stochastic motion is confined to constant energy surfaces, the steady-state solution will be non-zero only along $H = 0$. The other stochastic surfaces, which are without a source, will become depleted of electrons. Along $H = 0$, we can replace the source by $\Gamma \delta(J_\theta)$. Setting $\partial f/\partial t = 0$ and integrating over J_θ, we obtain the well-known flux relation $\Gamma = -D(J_\theta)\partial f/\partial J_\theta = $ constant. We may integrate once again to obtain the distribution function. The anode is modeled as a perfect

absorber of electrons; the boundary condition is then $f(J_A) = 0$, where J_A is the action value corresponding to the anode. Graphing $D(J_\theta)$ on a log-log plot indicates that $D(J_\theta)$ may be accurately fitted by a simple power-law expression: $D(J_\theta) = \Delta^2 \gamma(Q, L) J_\theta^{\nu(Q,L)}$, where $\gamma(Q, L)$ and $\nu(Q, L)$ contain the parametrization of $D(J_\theta)$ in terms of the equilibrium and wavelength parameters. For a wide range of Q and L we find $1.6 \lesssim \nu \lesssim 1.8$. The integration of the flux equation is now straightforward:

$$f(J_\theta) = \frac{\Gamma J_A}{(1 - \nu) D(J_A)} \left[1 - (J_\theta/J_A)^{1-\nu} \right]. \qquad (8)$$

Note that the distribution is proportional to the flux Γ, which is yet to be determined.

Leakage Currents

Integrating Eq. (8) from $J_\theta = 0$ to $J_\theta = J_A$ relates the flux Γ to the number of diffusing electrons: $\Gamma = (2 - \nu) D(J_A) J_A^{-2} \rho$, where ρ is defined by the integral of $f(J_\theta)$ from 0 to J_A. To calculate the actual leakage current, we must determine ρ. The diffusing population ρ is required to be equal to the globally stochastic fraction of the equilibrium electrons.

The calculation of ρ consists of a numerical integration over the allowed energy surfaces. A contribution equal to the local equilibrium density is made if a given energy surface is globally stochastic. The maximum value of ρ in our dimensionless units is 1.0, corresponding to global stochasticity on all available energy surfaces. Details on the calculation of ρ can be found in Ref. 10. For comparison with earlier experimental results and to obtain a useful measure of the leakage current, we normalise the leakage current $e\Gamma$ to the Child-Langmuir [11] current for the actual gap d. We obtain

$$\frac{I}{I_{cl}} = \frac{9}{2}(2 - \nu)Q^{-1/2} D(J_A) J_A^{-2} \rho(Q, \Delta, L). \qquad (9)$$

The plot in Fig. 2 compares our theoretical results (solid curve) to a simple fit to the experimental data of Orzechowski and Bekefi (dashed line). The circles are the
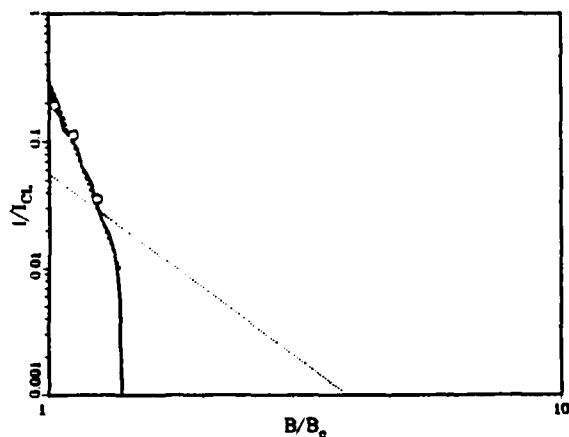
Fig. 2. Leakage currents I/I_{cl} versus B/B_c for $\Delta = 0.065$ and $L = 2.7$. The dashed line is a fit to the experimental results of Ref. 2 for their mechanical gap 0.54 cm. The dotted line is the theoretical prediction of Ref. 12. The circles are the result of a semi-numerical calculation.

result of a semi-numerical calculation in which we determine the mean inverse crossing time $\langle \tau_d^{-1} \rangle$ numerically to yield the semi-numerical flux $\Gamma_{num} = \rho \langle \tau_d^{-1} \rangle$. Also shown is the result of Mouthaan and Süsskind [12] (dotted line), an earlier attempt to calculate leakage currents in crossed-field devices. The agreement between both our analytical and semi-numerical calculations and the experimental results is very good. Similar curves are obtained that fit the remaining data of Orzechowski and Bekefi. Comparison of our results with their experimental data indicates that the characteristic wavelength of perturbations, normalized to the actual gap d, was an increasing function of the mechanical gap. Had the perturbations been a result of mechanical irregularities, the converse would have been true. For their mechanical gap of 0.54 cm, the characteristic wavelength, normalized to the actual (dynamical) gap, was approximately 2.7; the electric field perturbation was approximately 4.8% of the accelerating field. For their mechanical gap of 0.23 cm, the normalized wavelength was approximately 2.2; the corresponding transverse electric field was approximately 7.3% of the accelerating field.

It is clear from examining the theoretical curve that this analysis predicts a sharp cutoff at some value of B/B_c greater than 1 (1.3 in Fig. 2). The location of the cutoff can be calculated using the approximate relation for the stochasticity parameter given by Eq. (6). Setting S equal to 1 and replacing Q with $(B_{sc}/B_c)^2$, we find

$$\frac{B_{sc}}{B_c} = \left[1 + \frac{8}{L} \left(\frac{\pi \Delta}{\sqrt{2}} \right)^{1/2} \right]^{1/2} . \tag{10}$$

This relation defines a revised critical-insulating-field for magnetic insulation, which we call "B-supercritical" and denote by B_{sc}.

It is important to note that the above analysis pertains to the actual or dynamical gap d, whereas the authors of Ref. 2 calculated B/B_c with the claim that the actual gap was nearly the mechanical gap. Recent experimental work [13] has initiated a quantitative investigation of the actual gap; their results indicate that the expansion of the electrode plasmas may significantly reduce the actual gap. With an understanding of the actual-gap dynamics, more accurate tests of this theory may be attempted.

Acknowledgments

References

1. M. P. Desjarlais and R. N. Sudan, Phys. Fluids 29, 1245 (1986).
2. T. J. Orzechowski and G. Bekefi, Phys. Fluids 19, 43 (1976); 22, 978 (1979).
3. L. Brillouin, Phys. Rev. 67, 260 (1945).
4. A. W. Hull, Phys. Rev. 18, 31 (1921).
5. A. N. Kolmogorov, Akad. Nayk SSSR Doklady 98, 527 (1954) [in Stochastic Behavior in Classical and Quantum Hamiltonian Systems, edited by G. Casati and J. Ford (Springer, New York, 1979), p. 51].
6. V. I. Arnold, Russ. Math. Surv. 18, 9, 85 (1963).
7. J. Moser, Nachr. Akad. Wiss. Gottingen Math. Phys. Kl. 2, 1 (1962).
8. B. V. Chirikov, Phys. Reports 52, 265 (1979).
9. L. D. Landau, Zh. Eksper. Theor. Fiz. 7, 203 (1937).
10. M. P. Desjarlais, Ph. D. thesis, Cornell University (to be submitted).
11. C. D. Child, Phys. Rev. 32, 492 (1911); I. Langmuir, Phys. Rev. 2, 450 (1913).
12. K. Mouthaan and C. Süsskind, J. Appl. Phys. 37, 2598 (1966).
13. Y. Maron, M. D. Coleman, D. A. Hammer, and H.-S. Peng, these proceedings.

ION BEAM OPENING SWITCH*

J.B. Greenly, G.D. Rondeau,
H.T. Sheldon, D.A. Hammer, P.L. Dreike**

Laboratory of Plasma Studies
Cornell University
Ithaca, N.Y. 14853

Abstract

Plasma opening switches (POS) have shown excellent characteristics in pulsed-power applications. Proposed POS scaling predicts that the fastest opening time for a given conducted current should occur using a high-velocity, low density plasma as the switch medium. The Ion beam opening switch (IBOS) uses a charge-neutral ion beam of 100-300 kV, ≤ 120 A/cm^2 as the switch "plasma". Its velocity of 200-600 cm/μs and density of $\sim 10^{12}$/cm^3 make this a very fast, low-density plasma compared with typical ~ 10 cm/μsec and $\sim 10^{13}$/cm^3 POS plasmas. The IBOS has conducted ≥ 70 kA flowing in a parallel plate transmission line driven by a 4 Ω pulser. IBOS opening time is load dependent being < 4 ns into a 15 nH and about twice as long into an electron diode load. However, switch impedance is not zero while current is carried, and rise to $\leq 3\Omega$ near peak current. Current conducted before opening is not linear with either injected ion current or switch area. The results suggest that electron current conduction occurs in a narrow channel of ≤ 1 cm axial length. In this experimental geometry, replacing the IBOS with a standard POS gave essetentially identical behavior, except: first, an order of magnitude less injected flux was required to conduct a given current with the POS than with IBOS, corresponding to similar injected plasma densities for the two types of switches. Second, clear evidence of $\vec{J} \times \vec{B}$ motion of the POS current was seen, while none was evident with IBOS. We are developing a model of this switch in which electrons conduct current by $\vec{E} \times \vec{B}$ drift, that is a self-consistent Hall current in the self-magnetic field of the line.

Introduction

Plasma opening switches (POS) have been shown to be of great interest to the continued development of pulsed power[1]. In the shortest pulse application these switches are intended to carry large currents (>1 MA) and then open in times of order 10ns or less. They may be able to provide large gains in voltage and power into a load by opening while current is flowing in an inductance "charged" by a standard pulsed-power generator. A POS is made by injecting a flowing plasma through one (perforated) electrode usually the anode of a magnetically-insulated vacuum transmission line, usually in coaxial geometry. When a high power pulse propagating down the line arrives at the location of the plasma the current is initially short circuited through the plasma until the current reaches a certain level, at which time the impedance of the plasma suddenly rises to a high value (i.e. the switch "opens"). A model based on plasma erosion, or the sweeping out of plasma from the gap of the transmission line as the current increases, has been developed. This model, called the plasma erosion opening switch (PEOS)[1], predicts opening of the switch to high impedance as magnetic insulation is established. This model predicts that the current carried by the switch plasma, before opening begins and voltage appears across the line, is proportional to the flux of plasma ions reaching the cathode. Also, the opening rate, once this "conduction" current is exceeded, is inversely related to the plasma density. Thus, to make an effective POS, the PEOS model determines the required plasma flux for a given current to be conducted. Furthermore, it indicates that fastest opening should occur when that flux is provided by a high velocity, low-density injected plasma.

Previous POS experiments have typically used plasma sources of $\sim 10^{13}$ cm^3 density and 10-20 cm/μs velocity. In order to test the PEOS scaling predictions, we have performed an experiment in which the injected plasma is a nearly charge - and current-neutral ion beam, usually protons of ≥ 400 cm/μs velocity (≥ 100 keV) and about $\sim 10^{12}$/cm^3 density.

A second reason for interest in this experiment is the expectation that such high plasma ion velocities should eliminate $\vec{J} \times \vec{B}$ motion of the switch plasma during conduction since the ion larmor radius is always larger than the line gap.

Description of the Experiment

The experiment, called an IBOS, for ion beam opening switch, is shown in Fig. 1. A flat parallel-plate transmission line, 10 cm wide with a 1 cm gap, was pulsed in negative polarity so the ion beam from a simple planar magnetically insulated ion diode [3] could be injected through a 10 cm x 10 cm area of the grounded line anode. The line was magnetically insulated at $\leq$ 10 kA, to the highest voltage, -450 kV, applied. The inductance between the output of the 4Ω OMNI II water pulse-forming line and the switch region was -150nH, while the load inductance was -15 nH. Up to 12 kA of injected ion flux was measured by the array of 15 biased charged collectors mounted in the switch cathode.

The beam uniformity was better than ± 30% over the switch area. The ion beam pulse lasted >200 ns, and the line current arrival time could be varied throughout this pulse. To compare the properties of IBOS with a typical POS, the ion diode was replaced by a standard Mendel-type [2] plasma gun placed 20 cm from the line cathode.

Experiment Results

The ion beam did produce an excellent opening switch into diode loads. Figure 2 shows an IBOS shot using a blunt carbon-cathode electron diode load of about 4Ω. The load impedance was infinite (electron emission did not begin) until the switch, and load, voltage reached -150 kV. The downstream (load) current then rose rapidly in about -10 ns, while the upstream current in the line inductance dropped somewhat, adding an L$\dot{\text{I}}$ voltage of $<$ 100 kV at the switch. Almost all of the current was diverted to the load after opening. It is notable that the amount of current conducted with negligible voltage across the switch was quite small, perhaps 10^-15 kA, although in this shot the injected ion flux was 11-12 kA. The PBOS model would predict a conduction current of at least 40 times the ion flux (if the ions are all protons). This result was universally observed with IBOS shots: the conduction current before switch voltage appeared in excess of the -10 kV inductive voltage due to $\dot{\text{I}}$ in the switch was quite small, and far below the bipolar-flow ratio characteristic of PBOS model behavior and previous POS experimental results. When IBOS was

used with a short-circuit (15nH) load, load current began very early and very little switching could be produced, as would be expected since load voltage appears so early. These results were anticipated, since bipolar flow with 200kV injected ions would require 200 kV counter flowing electrons in the switch gap; thus PBOS type "conduction" current would not be reached until the switch voltage approached 200 kV. Even at this voltage however, the observed switch current was well below the bipolar value except when the switch axial length was reduced to $\leq$ 1 cm, as shown below.

When we replaced the ion beam with the plasma gun, our POS results did agree qualitatively with previous experiments in terms of ratio of (low voltage) conduction current to plasma ion flux. Figure 3 shows a POS shot into the short-circuit (15 nH) load in which a conduction current of about 25 kA was carried with a plasma flux of about 0.3 kA.

Since IBOS nevertheless gave excellent switching into a typical diode load which did not "close" and begin to carry current until a certain voltage was reached, we investigated this behavior further. In order to simplify the effect of the load on the switch-circuit behavior, we made a series of shots in which the electron diode was replaced by the 15 nH short-circuit with an added series surface-flashover switch which broke down at about 200 kV. Thus, the load began as an open circuit, as does a diode load, but after this load "turned on", it had a simple 15 nH impedance instead of the more complicated time-decreasing impedance of a diode load. A typical IBOS shot with this load is shown in Fig. 4. The switch (upstream) current and voltage rise as with the diode load until the surface switch closes. Then the load current rises very rapidly, with full current diverted to the load in as little as 4 ns. Again, a negative $\dot{\text{I}}$ can appear upstream during opening, generating inductive voltage which appears as the plateau in V_{sw}. After opening, the voltage drops to the low level characteristic of L $\dot{\text{I}}$ into the 15 nH load.

When a POS was used with the same load, Fig. 5, the switching waveforms were indistinguishable from IBOS. However, the plasma flux required for a given current conducted before the surface-switch breakdown voltage was reached was again an order of magnitude less for

POS than for IBOS. With this load the scaling of current at the time of opening with IBOS and POS flux was investigated. Results are shown in Fig. 6. The switch current did not scale linearly with flux for either IBOS or POS. Both scale more nearly with the square root of the flux. Although the flux differed greatly between IBOS and POS for the same switch behavior, the density as determined from measured flux and velocity for similar IBOS and POS shots, was often within a factor of two of agreement.

We also investigated the scaling of IBOS and POS switch current with the axial length of the switch, by masking off various parts of the anode extrance area, keeping the incident plasma or beam flux density constant. Results are shown in Fig. 7. In both IBOS and POS, the current carried before flashover switch voltage was reached was far from proportional to switch length (area) except for very short switches. One possible interpretation of this result is that the switch current is being carried in an axially very narrow channel, so when the switch plasma axial length is greater than this channel thickness, very little additional current is carried by the rest of the plasma. The experimental results would imply current channel axial length of the order of 1/2-1cm. If this is true, a two dimensional model of the switch behavior is certainly required, and the simplest PEOS model cannot entirely be expected to explain the behavior of these switches.

We are developing a new opening switch model based on a self-consistent $\underline{E}$ x $\underline{B}$ Hall current channel cross the switch plasma gap. This channel results from the electric field of an axial charge separation due to V x B force on the current carrying electrons, and the self-magnetic field of that current. A cathode sheath is required to inject electrons at the self consistent drift velocity into the Hall channel, giving a relation between the switch (sheath) voltage and switch current. In particular, if the Hall channel thickness is c/wpe, the collisionless skin depth, the switch (sheath) voltage becomes equal to the axial Hall voltage, which varies inversely with the plasma density and proportional to switch current squared. Thus at a given switch voltage, e.g. the voltage at which the surface switch broke down in our experiment, this model predicts switch current proportional to the square root of the plasma

density. The collisionless skin depth in our experiments was $\leq$ 0.5 cm. A detailed presentation of this model will appear in a future publication. This model gives switch impedance history, and scaling with switch length and plasma parameters, that agree with both our IBOS and POS experiments.

One further difference between IBOS and POS results was observed which agreed with the expectation that IBOS might be immune to $\underline{J}$ x $\underline{B}$ motion. No damage was ever observed beyond the downstream boundary of the beam entrance area with IBOS, while with the POS, one shot sufficed to melt a mylar sheet defining the anode entrance aperture for a distance of 2 - 4 cm past the downstream edge of the switch region. This damage is presumably due to current-carrying electrons accelerated across the switch before and during opening. An estimate of the distance the POS plasma should be pushed downstream by $\underline{J}$ x $\underline{B}$ indicates that if the current were being carried by the full mass of the switch plasma, very little motion should occur, whereas if the current channel were only 1 cm long, motion should be comparable to that observed. However, some "pinching" of the current in the direction across the 10 cm width of the line is also evident, which might complicate an estimation of the expected motion.

1. P.F. Ottinger, S.A. Goldstein and R.A. Meger, J. Appl. Phys. 56, 774 (198)

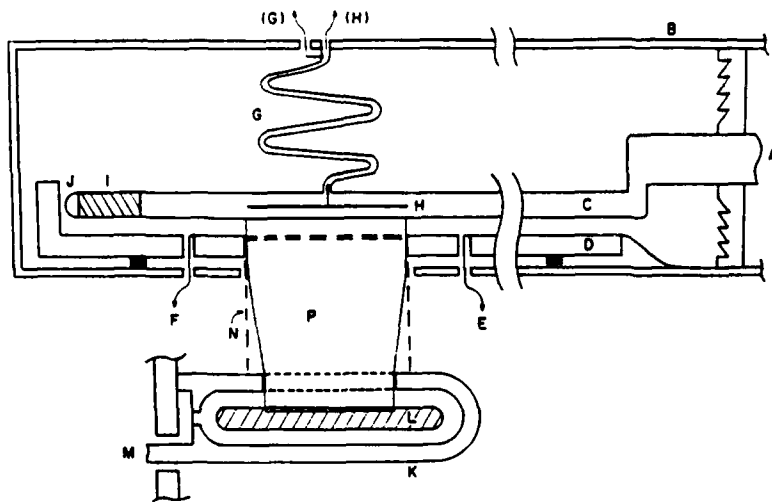2. C.W. Mendel et al., Rev. Sci. Inst. 51, 1641 (1980)

Fig. 1 (A) OMNI II, 4Ω, kV, 100 ns; interface to (B) vacuum chamber, driving (C) switch line cathode and (D) anode, 10 cm wide plates. Diagnostics: (E) upstream and (F) downstream current; (G) inductive divider for switch voltage; (H) multi-aperture ion beam current monitor. Load (I) surface-flashover series switch; (J) electron diode. Ion diode: cathode (K); anode (L) driven SNLA Marx, 300 kV, 10Ω, magnetically insulated by (M) capacitor bank. Flux-excluding tube (N) transports ion beam (P).

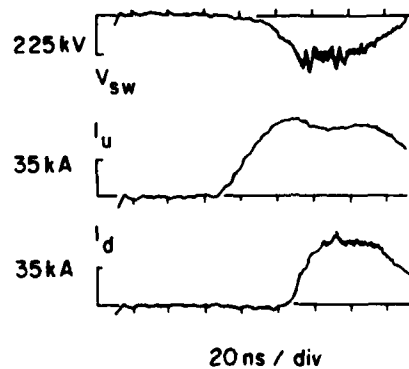Fig. 2. IBOS switching into an electron diode load. Vsw is the inductive voltage divider, I_u is sum of upstream $\dot{B}$ loops, and I_d is sum of downstream $\dot{B}$ loops.
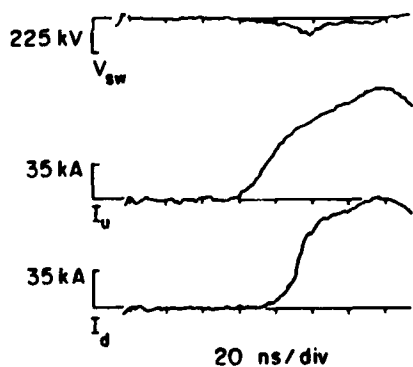
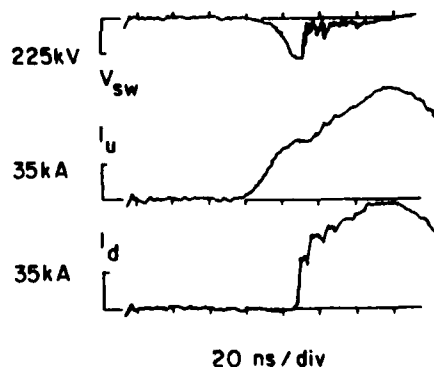Fig. 3. POS switching into a 15 nH load.

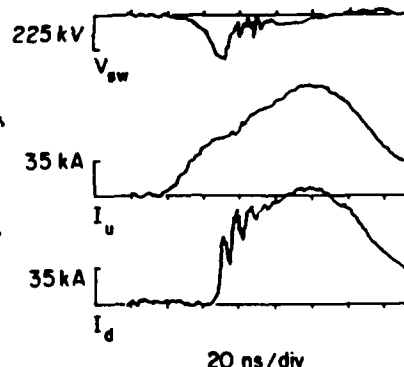Fig. 4 IBOS switching into 15 nH plus series surface switch.

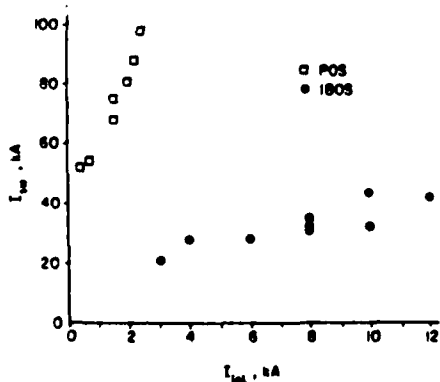Fig. 5 POS switching into 15 nH plus series surface switch.

Fig. 6 Switch current at opening versus injected flux for POS and IBOS.
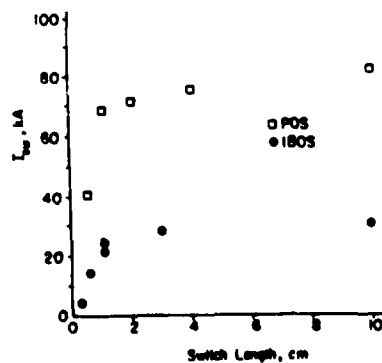
Fig. 7 Switch current ($I_{sw} = I_u$) at opening versus switch axial length for POS and IBOS.

Magnetically Insulated Ion Diode With a Gas-Breakdown Plasma Anode*

J.B. Greenly, M Ueda, G.D. Rondeau and D.A. Hammer

Laboratory of Plasma Studies Cornell University
Ithaca, New York 14850

Abstract

An active anode plasma source has been operated on the LONGSHOT annular magnetically insulated ion diode. This source uses an inductive voltage from a single turn coil to break down an annular gas puff produced by a supersonic nozzle. The resulting plasma is magnetically driven toward the radial insulating magnetic field in the diode accelerating gap and stagnates at a well-defined surface after about 300 ns to form a plasma anode layer defined by magnetic fields. An ion beam is then extracted from this plasma layer by applying typically a 150kV, 1 µs pulse to the accelerating gap. Optimization of the timing of the gas puff, the plasma production discharge and the high voltage pulse has resulted in 1 µs duration 75-150 keV ion beam pulses with >100 A/cm^2 peak ion current density over an area of about 400 cm^2. Up to 5J/cm^2 has been collected by a 4 cm^2 calimeter. The diode impedance history can be varied so that rising, flat, and falling voltage pulse waveforms can be produced. Streak photographs of beamlets impinging on a scintillator and time integrated targets both show beam divergence angles $\leq 3°$, but under certain operating conditions, large excursions ($~25°$) in mean aiming angle on time scales of 20-200 ns. These and other operating characteristics of the gas-beakdown diode are discussed.

Introduction

Magnetically insulated diodes (MID's) have proven to be very useful intense ion beam sources in applications ranging from Inertial Confinement Fusion at the $>10^{12}$W level [1] to materials science research at a power level of about 10^{10}W [2]. The ion source at the anode in these diodes has usually been a flashover plasma induced on a dielectric surface by the high voltage pulse that accelerates the ion beam [3]. Electrons which "leak" across the insulating magnetic field and impinge upon the surface are also believed to play a major role [4]. Such "surface flashover anodes" have several disadvantages, including:
1. The turn-on delay, especially for short pulses or at low voltages, can waste a substantial fraction of the power pulse delivered to the ion diode; 2. The large number of neutrals blown off the surface as part of the flashover process are believed to be responsible for the rapidly impedance characteristic of these diodes [7]; 3. Ion beams drawn from surface flashover plasmas tend to be a mixture of protons and heavier species, especially various charge states of carbon and oxygen and 4. The life of surface flashover anodes ranges from one pulse at the highest power levels [1] to perhaps a few hundred at the 10^9W/cm^2 level [2,7] due to the damage they sustain from electron bombardment.

There have been several attempts to provide an anode plasma ion source which does not suffer from these disadvantages, such as the plasma filled diode of Mendel [8], the plasma source used by Humphries et al [9] which is a direct ancestor of the source we describe here, and the actively driven surface flashover anodes (using an energy source independent of the main ion accelerating power pulse) of McClure [10] and Greenly [11]. Other possibilities in various stages of development are described in other papers in this conference [O-E-6, O-H-2 and 4, P-B-20, etc].

In this paper we describe a magnetically insulated diode with a gas-breakdown anode plasma ion source which improves upon almost all catagories of results obtained with a surface flashover anode when operated on the same pulsed power generator (LONGSHOT). The total ion output has been more than doubled. A variety of diode impedance histories including constant or even rising impedance can be selected by changing parameters of the source. Proton beams produced when H_2 gas is used show no impurity species, within the ± 10% ability of the foiled Faraday-cup measurement technique. Furthermore, the beam extraction can be made to begin coincident with the beginning of the voltage pulse. The diode was fired hundreds of times without damage or

replacement of parts. Only the divergence angle, 3°, was not improved over surface flashover diode results.

Clear correlation is seen between various aspects of the diode performance and measured anode plasma characteristics. For example, the ion beam current density is related to the anode plasma flux and to its position as determined by the magnetic field of the plasma source and diode. These dependences, along with the ion beam chacteristics, have led to an understanding of the source gap operation which will be discussed in future publications.

Description of the Gas-Breakdown Anode Plasma Source.

The principal components of the gas-break-down anode plasma source are shown in the LONG-SHOT diode in Fig. 1. The sequence of events for the system is as follows: The "slow" field coils are energized first, producing the quasi-static magnetic field configuration shown in Fig. 2. (Note that the space just in front of the fast coil is a relatively weak field region before the fast coil is pulsed). Next the puff valve on the diode axis is suddenly opened, and an annular gas puff is delivered to the volume in front of the fast coil (at 15 cm radius) by a supersonic nozzle. The axial puff profile is sufficiently sharp that the gas pressure in front of the middle of the fast coil can be up to 100 mTorr while the pressure in the ion diode accelerating gap 4 cm away (to the right in Fig. 1) is below 0.5 mTorr. At the optimum moment relative to the time of opening of the puff valve (a function of gas species), the preionizer is energized, followed about a microsecond later by the fast coil. The latter generates a loop volt-age of 17 kV (typical) which drives a current in the preionized gas cloud and rapidly breaks it down. The $J \times B$ force on the plasma current then drives the plasma toward the ion diode accelerat-ting gap. The plasma stagnates against the magnetic field produced by the slow coils, which field serves to magnetically insulate the accelerating gap of the LONGSHOT ion diode. The precise position of stagnation is determined by the relative sizes of the fast and slow magnetic fields and is designed to be near the axial posi-tion of the metal anode. It takes about 300 ns for the plasma to be driven to the stagnation

point under typical plasma source conditions. The high voltage pulse is then delivered to the accelerating gap.

Figure 3 shows the plasma flux observed on the source side of the stagnation point, as a function of time between pulsing the preionizer and the fast coil. By selecting this time in the range of about 0.2-1.0µs, it is possible to substantially vary the amount of plasma delivered to the accelerating gap. Varying the gas puff pressure in the range 30-70 mTorr, or the loop voltage over the range 14-23kV changed the plasma flux roughly linearly. The data in Figure 3 were obtained with biased Faraday cups. Double Langmuir probe measurements as a function of axial position across the stagnation point showed a factor of ten decrease over a distance of 3mm, from a peak density of $\sim 10^{14}/cm^3$.

Ion Diode Operation with the Gas-Breakdown Plasma Anode

Ion beam production by the LONGSHOT diode using the gas-breakdown plasma anode was monitored with arrays of single small-aperture biased (-200V) Farday cups, with a multiple-small-aperture 12 cm^2 biased Faraday cup, with a 4cm^2 calorimeter, with damage targets (both with and without shadowplates), and with a shadowplate-Pilot-B-Scintillator-streak camera combination to obtain time resolved beam optics information. We first consider the basic diode performance(impedance and output current density) obtained with the gas-breakdown anode plasma source, followed by results on the beam quality.

Diode Characteristics

By adjustment of the amount of plasma delivered to the diode accelerating gap, the time of arrival of the plasma relative to the application of the high voltage pulse from the LONGSHOT generator, and the magnitude of the insulating magnetic field, a variety of diode operating conditons could be achieved. Figures 4,5 and 6 show sets of data for pulses which illustrate the range of results that can be obtained. Each set contains inductively corrected diode voltage, total diode current, and two or more Faraday cup traces. They show that flat or even rising voltage waveforms can be produced by this ion beam source, in contrast to the typical falling voltage waveform obtained

using a surface flashover anode plasma ion source. Ion current extraction can be made to begin coincident with the arrival of the high voltage pulse as shown in Figure 5, or delayed relative to it as in Figure 4b and 4c. Ion beam pulses of 0.6 - 1µs above 70keV can be routinely obtained. In fact, the voltage pulses shown in Figures 4b and 6 are as long as "open-circuit" shots without injected plasma. Figure 6 shows that constant diode impedance could be maintained for long times with high ion output.

Beam uniformity better than ± 35% in both radial and azimuthal directions was obtained with Faraday cups. Faraday cups 1 cm apart agreed to ± 10%. Gas-puff and preionizer uniformity were critical to the attainment of this performance.

By averaging Faraday cup traces such as those in Figure 5, integrating the average over time and multiplying by 300cm^2 (out of the total 400 cm^2 to correct for radial profile), we estimate that $(1.5 \pm 0.5) \times 10^{17}$ ions with energies greater than 60 keV were produced. A 4 cm^2 calorimeter measured as much as 5J/cm^2 in the most energetic shots; this is consistent with 100 A/cm^2 for 0.5 µs, or 1×10^{17} 100keV ions over 300 - 400 cm^2. Since Faraday cups are likely to over-estimate the current density while the calorimeter-determined energy density is a lower limit because of surface blowoff from the high ion fluence, these numbers are consistent. It is then possible to estimate the ion current efficiency (ion current/total diode current). Without correcting for possible Faraday cup error, ion current efficiencies up to 70% for 0.5 µs or more have been obtained. A lower limit of 30% average efficiency for the whole pulse is given by the calorimeter.

Beam Optics

If plasma source conditions were set such that the extracted ion current density, j_i was < 60 A/cm^2, or if the high voltage pulse was applied to the accelerating gap before any plasma reached it, streak photographs of beamlets passing through an aperture plate and impinging upon a Pilot-B scintillator showed beam divergence of <3° agreeing with time integrated shadowbox targets, and no time dependent beam aiming error. However, if $j_i \geq 60$ A/cm^2 at some time in some part of the diode, and plasma had been driven into the accelerating gap by the time

the voltage pulse arrived, substantial time-dependent beamlet aiming error occured at that location. The streaks then showed beamlet motion of 20-30° on a time scale of tens to hundreds of nanoseconds. Such aiming errors might be due to a time-varying uneven anode plasma surface. This behavior disappeared when screen mesh was attached to the anode contact forming a flat equipotential surface over the entire anode area.

Finally, we note two additional observations. Because the puff valve can, in principle, be filled with any gas, it should be possible to produce pure beams of many different ion species. In fact, we have produced more than 100 A/cm^2 beams using a nitrogen gas puff. No major diode components required replacement in over 700 shots with the gas-breakdown anode plasma source, confirming the possibility that this ion beam source is capable of reptitive pulse, long lived operation.

[1]   J.P. New VanDevender and D.L. Cook,. Science 232. 831 (1986)

[2]   W.K. Chu et al., Nucl. Instr. and Methods 194, 443 (1982)

[3]   See, for example, S. Humphries jr., Nucl. Fusion 20 1549 (1980) article.

[4]   D.J. Johnson et al., J. Appl. Phys. 58, 12 (1985)

[5]   D.S. Prono et al., J. Appl. Phys. 52, 3004 (1981)

[6]   J.B. Greenly and Y. Nakagawa, Cornell University LPS report #303, Oct. 1982.

[7]   R. Pal and D.A Hammer, Phys. Rev. Lett. 50, 732 (1983)

[8]   C.W. Mendel jr. and G.S. Mills, J. Appl. Phy. 53, 7265 (1982)

[9]   S. Humphries jr. et al., J. Appl Phys 51, 1876 (1982)

[10]   G.W. McClure et al., Sandia Report SAND82-0340, Sept. 1982

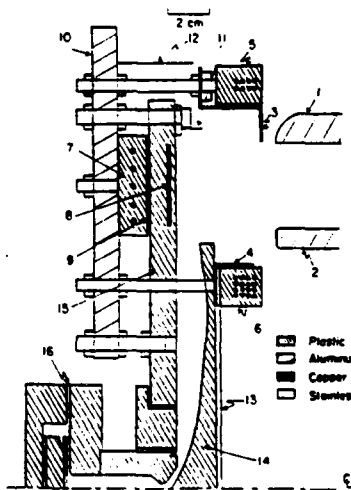[11]   J.B. Greenly et al., Cornell University LPS report #315

Fig. 1 Diode and plasma source components: (1) outer cathode, (2) Inner cathode, (3) Anode contact and outer field excluder for fast field, (4) Inner field excluder for fast field, (5) Outer diode insulating coil, (6) Inner diode insulating coil, (7) Back slow coil, (8) fast coil, (9) Back field excluder for fast field, (10) Diode support, (11) Preionizer support, (12) Mylar collar shield, (13) Stainless steel, (14) Front nozzle structure, (15) Fast coil insulator, (16) Puff value.
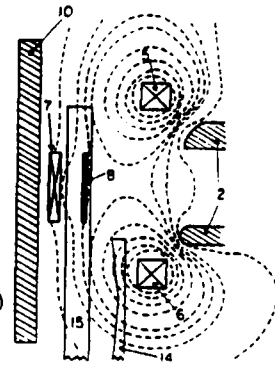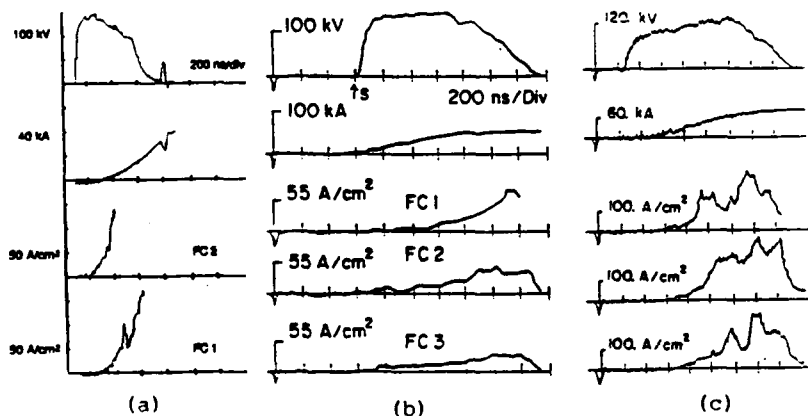
Fig. 2.

Fig. 4 (a) Diode voltage and current and Faraday cup traces for a standard flashover anode shot. (b) and (c), traces for two shots with the plasma anode, with different injection and timing conditions.
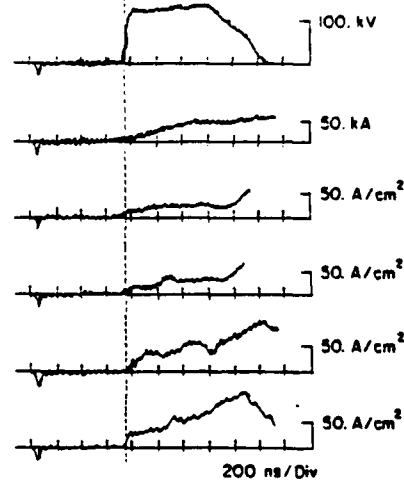
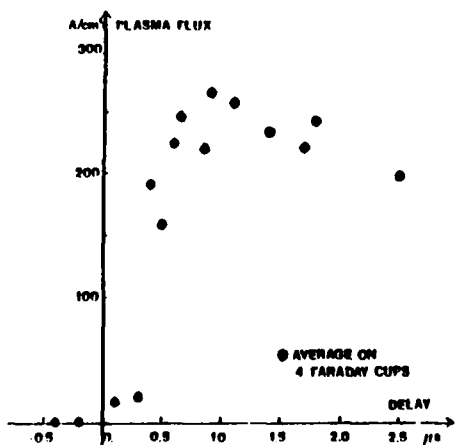Fig. 5 Traces for a shot with plasma injection timing giving prompt ion beam turn-on.

Fig. 3 Flux of plasma from fast coil as a function at delay between preionizer and fast coil firing.
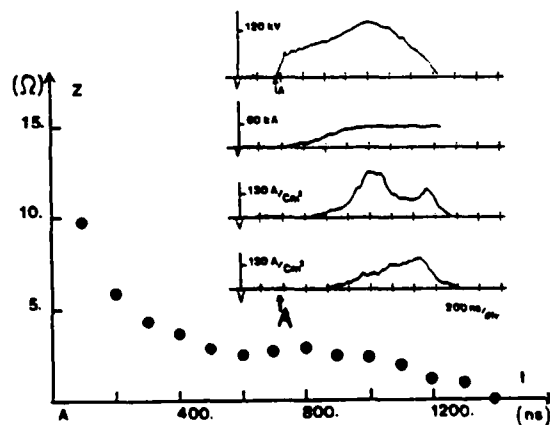
Fig. 6 Diode impedance versus time for the shot with traces shown.

INTENSE ION RING APPLICATIONS TO MAGNETIC FUSION*

D.A. Hammer, J.B. Greenly, P.D. Pedrow*,
E. Schamiloglu, and R.N. Sudan
Laboratory of Plasma Studies
Cornell University
Ithaca, N.Y. 14853

Abstract

The application of intense ion rings to the heating, stabilization and refluxing of Compact Toroid Plasmas is being addressed by two experiments, IREX and LONGSHOT. In IREX, ion rings containing up to 3×10^{15} 400keV protons have been trapped in an 8 kG magnetic mirror. Trapping is accomplished by the use of a fast (1 μs rise time) upstream mirror coil, and static fill or puffed hydrogen gas to allow prompt space charge neutralization. Trapped rings decay in about 5 μs principally due to a combination of energy loss and charge exchange on the background gas. In LONGSHOT, a rotating 150 keV proton beam containing up to 10^{17} particles is injected into a 2.5 m long preionized hydrogen plasma column in a >4.5 kG magnetic field to study the interaction of the ion ring with the plasma. Results from these two experiments are presented.

Introduction

The potential role of intense ion rings in magnetic fusion, for example, to heat, stabilize and/or reflux Compact Toroid Plasma configurations, is being addressed by two experiments at Cornell, IREX and LONGSHOT. More specifically, these experiments address the formation of ion rings by passing an ion beam from an annular magnetically insulated intense ion beam diode through a magnetic cusp, the trapping of such rings in a magnetic mirror configuration (IREX), and the merging of these rings with a Compact Toroid Plasma (LONGSHOT). This paper discusses the progress made in these two experiments since the last conference in this series [1]. In IREX, we have trapped up to 3×10^{15} 400keV protons in an 8 kG magnetic mirror. In LONGSHOT, we are studying the propagation of 150keV ion rings in a 2 1/2 m long preionized hydrogen plasma in preparation for an experiment to merge a proton ring with a compact Toroid Plasma.

IREX

The Ion Ring Experiment (IREX) is shown schematically in its present form in Fig. 1. The annular magnetically insulated diode shown in Fig. 1 is used to inject a >430 keV proton beam through a magnetic cusp produced by the superposition of the field from the solenoid surrounding the experiment, and the diode insulating field produced by the coil in the anode. The resulting rotating proton beam ("ring") has 80-90% of its energy in the transverse direction. Trapping is accomplished by injecting the axis-encircling proton ring through a fast risetime (1μs) upstream mirror coil capable of achieving a 1.4:1 peak mirror ratio, and reflecting the ring off a static 1.23-1.45:1 mirror located 1.5m downstream. In order to provide space charge neutralization for the ions, the rings are propagated and trapped in a static >50mTorr H_2 gas fill, or in gas puffed only in regions of spatially varying magnetic field. The $\leq 10^{-4}$ Torr ion diode region is separated from the gas filled region of the experiment by a 2μm mylar foil. The protons are detected using magnetic probes, Faraday cups, heat sensitive "witness targets", and CR-39 particle track detector material.

Initial Trapping Experiments

The earliest trapping experiments [2] were performed with 1.23:1 static downstream mirror, a 1.22:1 peak pulsed upstream mirror, and a relatively weak but reproducible proton ring containing typically 2×10^{15} protons on its first pass through the mirror. The pulsed power generator driving the ion diode was the 7Ω, 100 ns. Neptune generator we have previously described [3]. The observed diamagnetism of the injected rings in the middle of the mirror ($z = 136$ cm) was up to $\delta B/B_o$ of about 0.01, where B_o, the applied magnetic field, was typically 8 kG.

In general, hydrogen fill pressures above 100 mTorr gave good propagation, reflection and trapping, while fill pressures below 50 mTorr

gave poor results. Good trapping was characterized by detectable ion rings ($\geq 0.5 A/cm^2$) for 6-8 passes of the ring through the length of the mirror, a time of about 4 μs (about 50 times the ion cyclotron period). The estimated initial number of _trapped_ protons (i.e. - reflected off the downstream and then the pulsed upstream mirrors) was typically 4×10^{14}, decreasing to 2×10^{13} on the eighth pass. The particle loss is believed to have been due to a combination of charge exchange and mirror losses, the latter because of the oscillatory upstream mirror (see Fig. 3, upper trace). A data composite for a typical ion ring trapped in a static hydrogen fill was shown in Ref. 2. Here (Fig. 2) we present a data composite for a trapped ring in which localized gas clouds were produced in the IREX experiment chamber by three puff valves, two located in the transverse magnetic field region near the injector and one just outside the downstream magnetic mirror. The H_2 gas pressure profile for the trapped ring shown in Fig. 3 is presented in Fig 4.

Puffed gas experiments were performed with two purposes in mind: 1.) to determine what regions of the experiment required gas, and at what pressure, to trap a ring, and 2). to increase the ring lifetime with respect to charge exchange losses by eliminating the gas where it was not needed. The Faraday cup traces in Fig. 3 show a detectable ion ring up to nearly 4μs, about the same duration as with a ≥ 100 mTorr static fill during these initial trapping experiments. When the peak of the puffed-gas profile in the cusp region was >75 mTorr, there was only modest degradation of the ring injected into the IREX mirror region, as determined by a decrease in the number of injected protons and by additional spreading of the ring. When the gas puff peak was reduced to 40-75 mTorr, the injected ring peak diamagnetism at z = 136 cm was reduced by a factor of three, its width increased by 50%, and the estimated number of particles decreased by a factor of four, relative to the ring shown in Fig. 2. It was determined that gas was needed throughout the region of nonuniform magnetic field at the injector end of IREX. The strength of the rings reflected from the downstream mirror (as determined by the peak current density of the reflected ring at z = 136 cm) was also affected by the gas puff pressure, but only up to 15-20 mTorr, above which no further increase in

ring strength was obtained. Below 15 mTorr, the reflected ring current density was roughly linearly dependent on puff gas pressure. No increase in trapped ring lifetime was seen in these experiments. This is probably because of the poorly crowbarred upstream mirror in these initial experiments (see upper trace in fig. 2), and the fact that scattering and charge exchange probably were not decreased by more than a factor of 2 - 3 using the puff gas profile shown in Fig. 3.

Experiments with Stronger Injected Rings

The injected rings used for the initial trapping experiments were optimized for reproducibility. An additional series of experiments [4] was performed in which the number of injected protons was optimized within the capabilities of the 7 Ω pulsed power generator then being used. In addition, the downstream magnetic mirror ratio was boosted to a maximum of 1.45:1, and the pulsed upstream mirror was improved by both a greater peak mirror ratio, 1.4:1, and a better crowbar. This revised magnetic field configuration, which is the one shown in Fig. 1, has been used only with static hydrogen fills. Injected rings of up to $\delta B/B_o = 0.04$ were obtained at z = 136 cm. With the 1:45.1 downstream mirror, up to 90% of the protons were reflected, producing a reflected ring $\delta B/B_o$ of more than 0.02 at the same central location. Since the magnetic probes that measure δB are shielded from the ring diamagnetism after two or three bounces by currents induced in the beam-formed plasma, we have had to rely on magnetically insulated, biased (-200V) Faraday cups to monitor the strength of trapped rings. Figure 4 shows sample data obtained from a trapped ring. Note that the Faraday cup is collimated and aimed to view only downstream moving rings. At least seven distinct ring current density peaks are visible on the signal, indicating that many round trip passes through the mirror, or fourteen mirror reflections, during its lifetime. Notice that the magnetic probe signal peaks drop off more quickly than the Faraday cup peaks. The peak current density of the entering ring, cut off in the trace shown was about $20 A/cm^2$. Notice that the magnetic probe singal peaks drop off more quickly than the Faraday cup peaks. In the better shots in this series, 3×10^{15} or more protons (≥ 200 J) were estimated to be trapped in

the magnetic mirror, with life times (using 75 -
100 mTorr of H_2) of 4-5 µs. Two more complete
data sets of a trapped ring from which such
numbers can be obtained are shown in ref.4. The
ensemble of such trapped ring data supports the
hypothesis that once the ring is trapped (i.e.-
after the first bounce off the upstream mirror),
charge exchange losses are responsible for the
decay of the ring. (See ref. 4 for details).
Finally notice that Fig. 4 suggests that in addi-
tion to the clear successive peaks of the ring
bouncing in the mirror, there is a uniform few
A/cm^2 "background" ion ring filling the entire
mirror after the second bounce. These two com-
ponents appear to decay at the same rate, as they
should if charge exchange is the loss mechanism.

Experiments with an Upgraded Generator

A third trapping run with the ion diode
driven by a 3Ω version of the Neptune generator
is presently in progress on IREX using static
hydrogen gas fills. Although the upstream mirror
has not yet been used, we have seen current
densities of injected rings and rings reflected
off the 1.45:1 downstream mirror at least twice
as large as in the previous run, as illustrated
by the Faraday cup traces shown in Fig. 5. The
peak current density shown implies a ring of peak
AB/B_0 of order 0.1, and is consistent with dia-
magnetic signals. This injected ring is
reflected from the downstream mirror as well as
weaker rings were, so we expect soon to be able
to study trapped rings of at least double the
previous current and energy.

LONGSHOT

The LONGSHOT II proton ring - plasma
interaction experiment is shown schematically in
Fig. 6. The LONGSHOT II injector with a
preionized anode plasma ion source (described in
detail in a paper by Greenly, Ueda, et al. in
this conference) produces an annular beam
typically containing more than $_{-}10^{17}$ >60keV
protons ($\geq$ 1 kJ). This beam is injected through
a cusp-like magnetic field into a 2.5m long, 15
cm diameter, preionized hydrogen plasma, produced
by a Z-discharge in the presence of >4.5kG
solenoidal magnetic field. To form the plasma, a
damped oscillatory circuit (C=100µF, L=3.2 µH, R
= 50mΩ) drives current between annular stainless
steel electrodes separated by about 2m in a

puffed neutral hydrogen fill of about 5 mTorr for
one half cycle (65 µs), after which it is crow-
barred. The afterglow plasma into which the ion
ring is injected has been determined by double
Langmuir probes and a microwave interferometer to
be a peak density of $10^{14}/cm^3$ and a temperature
of about 3eV. An 80% transparent, fine stainless
steel mesh stretched across the entrance to the
interaction region (at z=20cm) and "grounded" to
the drift chamber walls prevents injector
operation from being affected by plasma drifting
into it from the Z-discharge.

Experiments with this ring-plasma have
recently begun. Early results indicate that the
ring is entering the plasma, and the diamagnetism
of the ring can be seen on axis in the plasma
near the injector. The magnetic signals decrease
rapidly in 1m of axial distance through the
plasma. The magnetic signal outside the ring
radius at the vacuum wall shows strong evidence
of induced plasma current, and oscillatory
signals persist after passage of the ring.
These experiments will study the ring-plasma
interaction, looking in particular for evidence
of slowing of the ring axial velocity by coupling
ring energy to magnetosonic waves in the
plasma.[5]

[1] J.B. Greenly et al., Proc. Fifth Int. Top.
Con. on High-Power Particle Beams, R.J. Briggs
and A.J. Toepfer, eds. (San Franisco, 1983),p 299
[2] P.D. Pedrow et al., Appl. Phys. Lett. 47,
225 (1985).
[3] P.L. Dreike et al., Phys. Fluids 25, 59
(1982).
[4] J.B. Greenly et al, Phys. Fluids 29 908
(1985).
[5] R.N. Sudan and P.M. Lyster, Comments Plasma
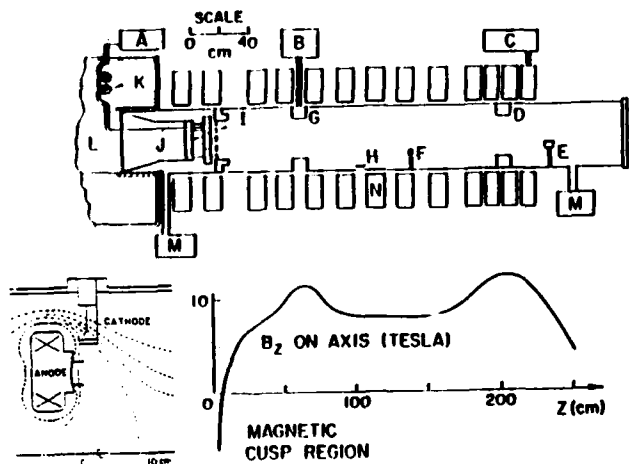Phys. Controlled Fusion 9, 35-44 (1984).

Fig. 1. IREX system, showing (A) capacitor bank supplying diode insulating magnetic field; (B) capacitor supplying (C) pulsed upstream mirror; (D) power supply for (E) solenidal field; (F) supplemental downstream mirror coil; (G) typical Faraday cup location;(L)Neptune generator supplying ion diode anode and (N) cathode with 2μm foil. Net applied magnetic field on axis is plotted below. Diode detail is also shown.
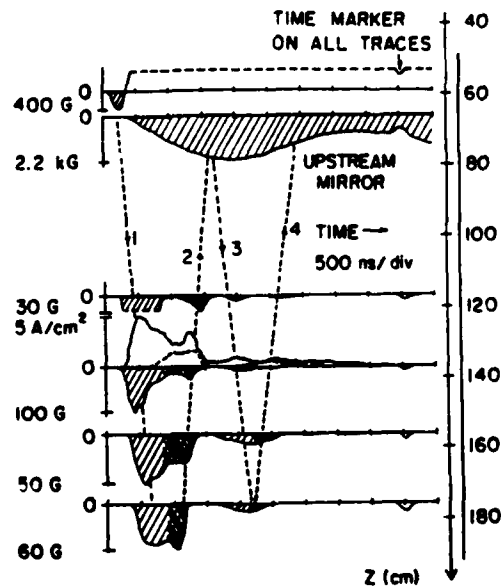
Fig. 2 Data for an IREX shot into puffed gas. All traces are 500ns/div; the upstream gate mirror strength is shown. Other traces are ion ring diamagnetic signal N (shaded, below the abcissas) at axial locations indicated at right. The two traces above the absissa the the 136 cm position are signals from Faraday cups collecting (solid line) all ring ions, and (dashed line) only upstream-moving (reflected) ring ions.
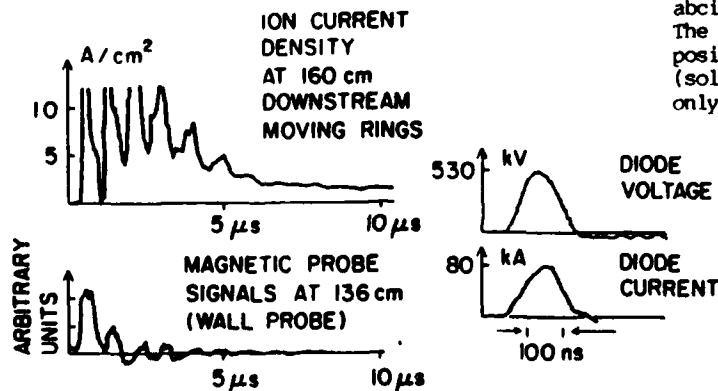

Fig. 4 Ion ring trapping with 7 Ω injector pulse shown by diode voltage and current traces. Ion current density at 160 cm axial position, measured by Faraday cup, and ring diamagnetic signal at the vacuum wall, showing rapid shielding of the ring self-field by induced currents in the ring-formed background plasma.
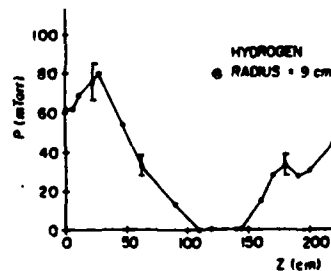
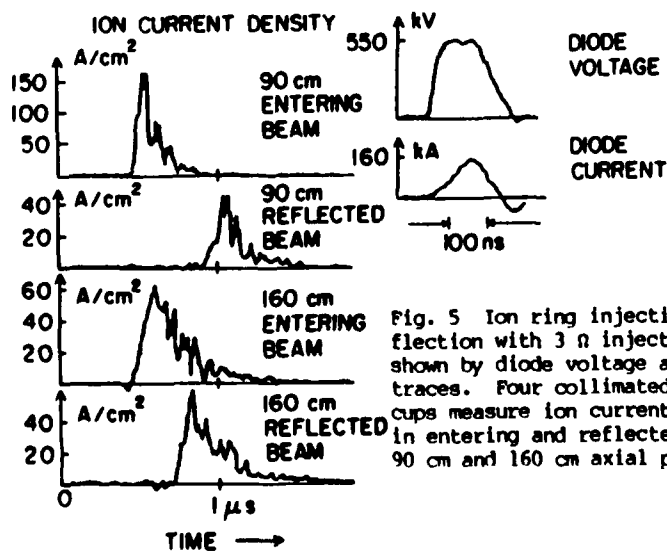Fig. 3 Puffed-gas pressure versus axial position for shot of Figure 2

Fig. 5 Ion ring injection and reflection with 3 Ω injector pulse shown by diode voltage and current traces. Four collimated Faraday cups measure ion current density in entering and reflected rings at 90 cm and 160 cm axial positons.
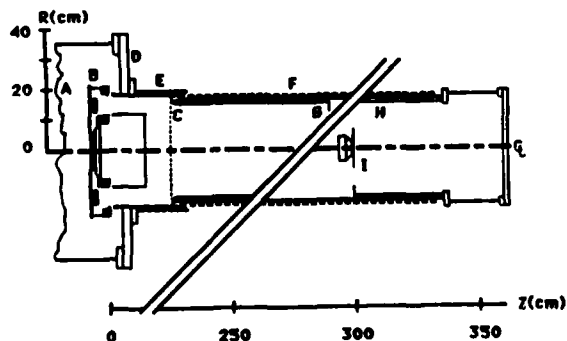
Fig. 6 LONGSHOT II- Proton Ring Plasma Interaction Experiment: (A) to generator; (B) ion diode; (C) grounded grid; (D) half-cusp producing aluminum plate; (E) proton orbit compression coils; (F) solenodial field producing coils; (G) ground Z-discharge electrode; (H) high-voltage Z-discharge electrode; (I) puff valve for Z-discharge fill.

PROPAGATION OF INTENSE ION BEAMS IN
STRONG MAGNETIC FIELDS AND BACKGROUND PLASMA

R. Kraft[*], B.R. Kusse and J.J. Moschella
Cornell University, Ithaca, New York

Abstract

The dynamics and propagation of an intense
ion beam under varing magnetic field and back-
ground plasma conditions have been studied in a
series of experiments. The 70 nanosecond (fwhm)
beam consisted of 8 KA of 360 KeV protons. The
first set of experiments investigated theoretical
models for ion beam propagation and neutralization.
Conventional diagnostics and a new method for in-
terpreting biased charge collector signals were
used. The second study concerned the focusing of
an intense ion beam as it propagated from a field
free region into a strong magnetic solenoid. The
third set of experimants concentrated on the ob-
servation of microwaves produced by ion beam-
plasma interactions.

Experimantal Apparatus

The experimantal apparatus is shown in Fig. 1.
The ion beam was produced by a planar, race track
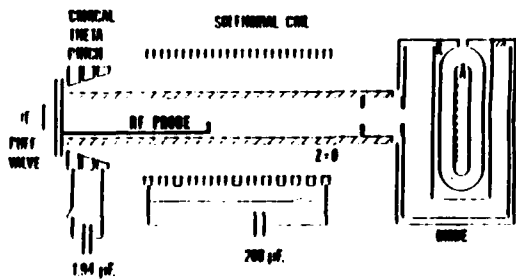type, magnetically insulated diode driven by a

Fig. 1 Experimental Apparatus

marx generator and pulse forming network. The pro-
ton beam had a 10 cm x 13 cm cross-section which
could be collimated down to a 4 cm diameter by two
aperture plates. After collimation the beam enter-
ed a 1 m drift region where axial and transverse
magnetic fields could be applied. A conical θ-
pinch plasma gun was located at the downstream end
of this drift region and was used to provide a pre-
ionized medium into which the beam could be propa-
gated. A puff gas valve located in the plasma gun
could be fired without voltage on the θ-pinch coil
to establish an adjustable, background neutral
pressure in the drift region.

Beam Propagation and Neutralization

Theoretical Picture   It has been proposed
that the ion beam, as it initially leaves the
cathode, picks up a neutralizing electron distri-
bution which is composed of two delta functions,
one at zero velocity and one at twice the ion
velocity [1]. The total number of electrons
equals the total number of ions and the beam is
current neutralized. It is also essentially
space charge neutralized except for the over-
shooting electrons which establish a self-consis-
tent positive beam space charge potential.

This electron distribution is unstable and
is predicted to quickly thermalize into a drift-
ing Maxwelliam centered at the ion velocity [2,3].
This thermalization also lowers the beam space-
charge potential.

Biased Charge Collector   When used with in-
tense ion beams, the aperature of a biased charge
collector reduces the ion current drematically
but not enough to allow one to ignore space
charge effects in the region between the apera-
ture and collector. Including these effects in
an analysis, it is possible to develope a set of
I-V curves for a collector which allows determin-
ation of the neutralizing electron temperature as
well as the ion beam density.

The geometry of the collector is shown in
Fig. 2 and consists of aperature and collector
plates and a floating bias supply. The current
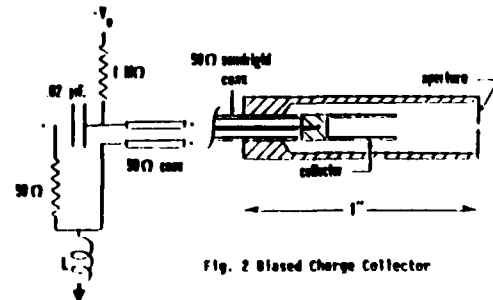
Fig. 2 Biased Charge Collector

signal is measured as a voltage across the 50 ohm
resistor. The incident beam is assumed to be com-
posed monoenergetic ions at density N_0 and vel-
ocity v_0 together with the neutralizing electrons
of equal density but characterized by a drifting
Maxwellian centered at v_0 and a temperature T_e.
The analysis for the I-V characteristic for the
collector proceeds from assuming that the apera-
ture plate attains the floating potential ϕ_f with

respect to the beam potential ϕ_b such that the incident ion and electron currents are equal. A fixed voltage, V_0, is applied between the aperature and the collector plates. The ions are assumed to be unperturbed and their current density and velocity are taken to be constant both inside and outside the collector. A space charge potential, ϕ_{ic} developes in the column between the aperature and collector plates to keep the electron and ion densities equal. Once ϕ_{ic} is known the electron distribution and current density at the collector plate can be determined [4].

In obtaining the electron distribution two conditions must be considered. If the collector potential $\phi_c = \phi_f - V_0$ is greater than the ion column potential ϕ_{ic} there are no reflected electrons at the collector and,

$$f_e = \begin{cases} N_0 \dfrac{m_e}{2\pi k T_e} \, e^{-m_e(v_0 - v^*)^2/kT_e} & v > 0 \\ 0 & v < 0 \end{cases} \quad (1)$$

where

$$v^* = [v^2 + 2e(\phi_b - \phi_{ic})/m_e]^{1/2}.$$

The ion column potential ϕ_{ic} is determined by requiring the integral of f_e to be N_0. If $\phi_{ic} > \phi_c$ then there are reflections and an additional term, n_r given by,

$$n_r = \int_0^{[2e(\phi_{ic} - \phi_c)/m_e]^{1/2}} f_e(v) \, dv \quad (2)$$

must be added to the electron density. Here $f_e(v)$ is the same function given by Eq. 1. For the case with $\phi_{ic} > \phi_c$ the column potential is again determined by requiring the electron density to equal N_0. Once ϕ_{ic} is known, the electron current and therefore the net current to the collector can be calculated as a function of V_0, v_0, T_e and N_0.

A set of curves showing the collector current as a function of the applied voltage is shown in Fig. 3 where T_e has been used as the parameter to
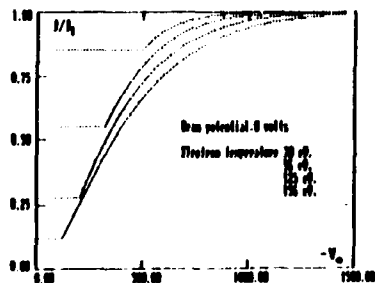
Fig. 3 Normalized Collector Current vs. Bias Voltage

generate the set. It can be seen that the curves behave as expected until V_0 reaches a critical value below which the space charge effects take

over and clamp the current. This critical potential depends on T_e and consequently curve fitting experimantal data allows a determination of T_e as well as N_0.

Measurements of ϕ_b and T_e A capacitive probe shown in Fig. 4 and a biased charge collector were used to measure T_e, N_0 and ϕ_b. The
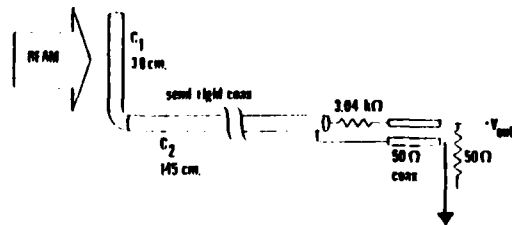
Fig. 4 Capacitive Probe

capacitive probe was designed to sit at the floating potential and ϕ_b was obtained from ϕ_f using T_e.

The experimental configuration was as shown in Fig. 1 with a permanent magnet and pole pieces to establish a localized, transverse field of approximately 200 G. Immediately down stream from this transverse field was a grounded conducting screen which could supply a new set of neutralizing electrons to replace those turned by the field. Potential and T_e measurements were made down stream from this screen and a plot of ϕ_f vs. distance from the screen is shown in Fig. 5. The
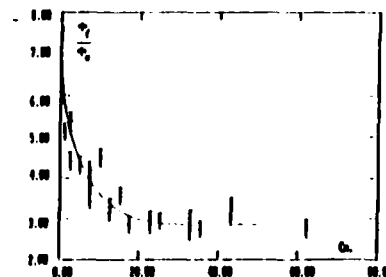
Fig. 5 Axial Variation of Floating Potential Normalized to Co moving Electron Potential

electron temperature, after thermalization, was measured to be 156 eV and the predicted decrease of the potential with distance is clear.

Collective Ion Beam Focusing

Because of the intensity of the neutralized ion beam considered in this work, magnetic focusing can require collective effects to adequately describe the phenomenon. Collective focusing using a short magnetic lens, where the focal point occurred in a field free region down stream from the lens, has been described by Robertson [5].

Our studies involved collective focusing of the
ion beam which occurred as the beam entered a long
magnetic solenoid.

Experimental Set-up The experiment was ar-
ranged as shown in Fig. 1 with the solenoidal coil
energized. The neutralized ion beam was collimat-
ed and propagated a short distance through a field
free region before it encountered the radial
fields of the solenoid. Within the solenoid the
biased charge collector was used to measure the
radial and axial profiled of the beam intensity.

Focusing Theory The collective focusing ef-
fect involves a co-operation between the beam ions
and their neutralizing electrons. Single particle
theories do not apply because of the large space
charge fields which can build up. The parameters
of the experiment were such that the electrons, by
themselves, could not have penetrated the radial
fields. The ions had no trouble crossing and
their space charge was able to add energy to the
electrons and pull them across. The ions, by
themselves, would have focused at a position in
the solenoid equal to the distance they could
travel in 1/2 a cyclotron period. As single par-
ticles the electrons wanted to focus in a much
shorter distance. As these events try to occur
radial electric fields built up resulting in a
common, collective focus inbetween the single par-
ticle electron and ion focal points.

This process can be described analytically by
assuming quasi-neutrality and following a calcul-
ation similar to Robertson's. The Lagrangians for
the electrons and ions are by,

$$L_\alpha = 1/2 \, m_\alpha v_\alpha^2 + q_\alpha(\bar{v}_\alpha \cdot \bar{A}) - q_\alpha \phi \qquad (3)$$

where the α subscript is used to indicate ions or
electrons, m is the mass, $q_e = -e$, $\bar{v}$ the vector
velocity, $\bar{A}$ the vector potential and ϕ the scalar
potential. Quasi-neutrality requires that the rad-
ial and axial motion of the electrons and ions be
equal and the following equations of motion result,

$$\frac{d^2 r}{dt^2} + \frac{e^2}{m_i m_e} A_\theta \frac{dA_\theta}{dr} = 0$$

$$\qquad (4)$$

$$\frac{d^2 z}{dt^2} + \frac{e^2}{m_i m_e} A_\theta \frac{dA_\theta}{dr} = 0$$

In Fig. 6a radial trajectories of monoenerget-
ic ions are plotted. As long as the ions remain
in the solenoid, multiple focusing is predicted.
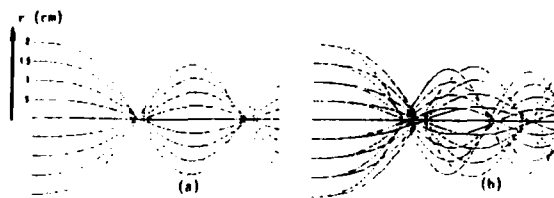In Fig. 6b the radial trajectories for ions with a

Fig. 6 (a) Monoenergetic Ions, (b) 25% Velocity Spread

velocity spread have been plotted. While the
first focal point is still present, subsequent
ones are smeared out and indistinguishable.

Focusing Measurements A biased charge col-
lector was used to measure the peak current den-
sity as a function of axial position within the
solenoid. The results are shown in Fig. 7a. On
the same graph is a similar measurement with no
solenoidal field to indicate the normal beam div-
ergence. Only a single focal point was observed.
The radial profile at the focal point is shown in
Fig. 7b. The measured and theoretical focal
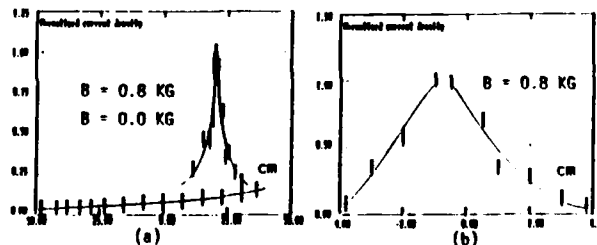
Fig. 7 Axial (a) and Radial (b) Variations
of Current Density

points as a function of magnetic field strength
are shown in Fig. 8.

The focusing effect was very dependent on the
ions being able to pull original neutralizing el-
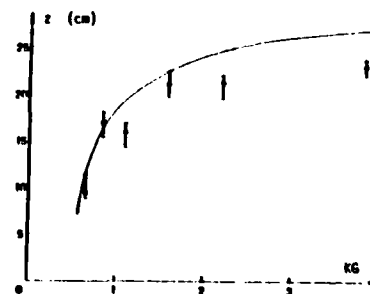ectrons all the was across the field. If it was

Fig 8 Focal Point vs. Field Strength

easier for the ions to pick up new electrons as a
result of an electron source in the radial field
region (i.e. a screen or wall bombardment by an

uncollimated ion beam) or a plasma prefill, the focus was destroyed.

Ion Beam-Plasma Microwave Interactions

It is believed that microwave interactions play a large role in ion beam neutralization and propagation [2,3]. In order to propagate an intense ion beam in vacuum a large degree of magnetic and electrostatic neutralization is required. This neutralization of the cold drifting ion beam is provided by an electron population whose velocity distribution evolves with time. Initially, as the electrons are drawn into the beam channel, they are cold and attain a drift velocity greater than that of the ions. As they overshoot the ions they are decelerated to approximately zero velocity. The two component distribution that results is unstable and quickly thermalizes by means of a microwave, two-stream instability to a hot, drifting Maxwellian centered at the ion velocity. If this neutralized beam then propagates through a background plasma further two-stream interactions can be present.

Observations of Instabilities Glass enclosed electrostatic probes were used to observe microwave signals both inside and outside the beam channel of the experiment shown in Fig. 1. The strong, broadband microwave signals from the diode made measurements during the initial neutralization and thermalization near the cathode impossible. Our cleanest measurements occurred when we stripped the beam of its neutralizing electrons and forced it to pick up new cold ones well down stream from the cathode. Under these conditions we were able to observe an interaction between the cold electrons and those in a background plasma.

This interaction was strongest when the beam was used to form a plasma from a neutral prefill and cold fast electrons were produced as the beam entered the magnetic solenoid. With this background plasma no collective focusing occurred. A plot of the frequency of the microwave signal as a function of the prefill pressure is shown in Fig. 9. The pressure was measured in the center of the center of the solenoid at the time of the beam pulse and can be converted to a plasma density through a rate of ionization equation. The frequency was determined by an x-band dispersive line and scaled with the background pressure and plasma density but was independent of magnetic field strength. The microwave signal strength as a function of position is shown in Fig. 10. The z = 0
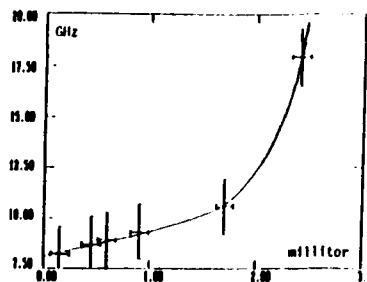

Fig. 9 Microwave Frequency vs. Neutral Pressure

position is under the first solenoid coil and the spatial growth indicated a convective instability
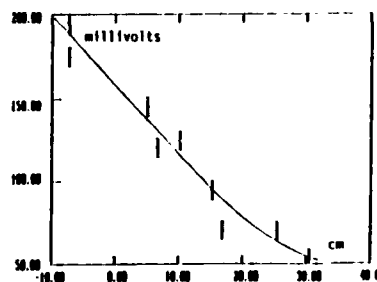
Fig. 10 Microwave Amplitude vs. Axial Position

with a 20 cm e-folding length.

Conclusions

Several experiments confirming the theoretical picture for neutralized ion beam propagation have been performed. Evidence of the production of fast, cold, neutralizing electrons that thermalize through a two-stream instability has been presented. Observations of the beam potential show its expected decrease as the electrons thermalize into a hot, drifting Maxwellian distribution. This distribution was measured using a new technique for analysing biased charge collector signals. No microwaves driven by the negative slope of the ion distribution were observed.

References

1. Humphries, S., Jr., Appl. Phy. Lett., 32, 792 (1978).
2. Humphries, S., Jr., Lockner, T.R., Poukey, J. and Quintenz, J.P., Phy. Rev. Lett., 46, 995 (1981).
3. Sudan, R.N., Appl. Phy. Lett., 44, 957 (1984).
4. Kraft, R., PhD. Thesis, Cornell University (1985).
5. Robertson, S., Phy. Rev. Lett., 48, 149 (1982).

*Present Address: Avco Everett Research Lab. Everett, Massachusetts

SPECTROSCOPIC INVESTIGATIONS OF THE ELECTRIC FIELD DISTRIBUTION AND ION MOTION IN THE GAPS OF HIGH POWER DIODES

Y. Maron

Laboratory of Plasma Studies, Cornell University, Ithaca, NY 14853
and Physics Department, Weizmann Institute, Rehovot, Israel

M.D. Coleman, D.A. Hammer, and H.-S. Peng[a]

Laboratory of Plasma Studies, Cornell University, Ithaca, NY 14853

Abstract

We have measured the electric field distribution across the gap of magnetically insulated intense ion diodes by observing the Stark shift of ion line-emission from the gap. The measured distribution yielded the time dependence of the actual diode gap, which decreased rapidly early in the pulse. The electron density distribution, inferred from the measured $E(x)$, was compared to one-dimensional calculations using the measured gap. Electrons were not confined to a well defined sheath near the cathode, but were spread significantly towards the anode, especially in vaned cathode diodes. These results serve to explain the enhancement of the measured ion current density over the space-charge-limited-value (calculated using the measured gap) that we observed. We also measured the velocity distribution parallel to the magnetic field lines of C^{++} and Al^{++} ions accelerated in the gap by observing the line Doppler-broadening. This velocity component was considerably smaller than the transverse proton velocity previously measured outside the diode.

Introduction

A true understanding of the operation of high power diodes requires measurements of their detailed properties, such as the actual accelerating gap spacing, the charge density distribution, the properties of the anode plasma, etc. However, the small gap spacings (typically $\leq 1cm$), and large applied electric fields (typically $> 1MV/cm$) make direct measurements within high voltage gaps very difficult. In this paper we report spectroscopic measurements of the electric field as a function of distance from the anode, and of the ion transverse velocities within a magnetically insulated ion diode. These measurements were made by observing spontaneous line-emission from ions excited in the anode plasma and accelerated in the diode gap. The electric field measurements reveal the actual accelerating gap spacing by locating the boundaries of the electric-field-excluding anode and cathode plasmas, rather than the position of the $\sim 10^{16} cm^{-3}$ or higher plasma boundaries observed in previous studies [1-3]. These measurements also give information about the electron density within the diode, which was found to be inconsistent with theoretical predictions assuming a well confined electron sheath near the cathode [4]. The mea-

sured gap spacing and electron density distribution serve to explain the enhancements we have measured in the ion current densities over calculated [4] values.

The measurements reported here were initiated as a result of a recent suggestion [5] that the electric field in the acceleration gap of a high power diode can be determined by measuring the Stark shift of line-emission from especially selected ions in the gap, as illustrated in Fig. 1a. Observations at different distances x from the anode yields the electric field distribution $E(x)$ across the gap. With this method, the measurement integrates over the field of view in front of the anode. The line-emission (collected parallel to the electrodes) is also Doppler broadened due to the transverse ion motion (parallel to the electrodes). Therefore, as discussed in [5], the measurement of the ion transverse-velocity distribution in the diode gap is accomplished by observing the spectral profile of a line which is negligibly shifted by the electric field relative to the Doppler broadening. We selected the $Al^{++}4d_{5/2} \rightarrow 4p_{3/2}$ emission (4529 Å) for the electric-field measurements, and confirmed it with the $Al^{++}4d_{3/2} \rightarrow 4p_{1/2}$ line (4512 Å). The $Al^{++}4p \rightarrow 3d$ (3602 Å) line as well as the $C^{++} 2s(^2S)3p \rightarrow 2s3s$ (4647 Å) line were used for the transverse velocity measurements.

Apparatus and Measurements

Experimental arrangement

We used the planar magnetically insulated diode [6] which is shown in Fig. 1b. The dielectric-anode surface was made up of a $140\times50\times1.6$ mm^3 polyethelene sheet with the long dimension parallel to the applied magnetic field B_z. Line-radiation emitted in the s direction from a planar surface parallel to the anode was directed by the mirror M to a lens L which focused it on the spectrometer input slit. Using the cylindrical lens CL, the spectrometer output was magnified, then focused on an array of seven fiber bundles placed parallel to the spectrometer slit. Each bundle transmitted the light to a PM tube, the trace of which was recorded with a temporal resolution of 8ns. The spatial resolution in the x-direction and the spectral resolution were 0.6 mm and 0.7 Å, respectively. Thus, seven points of the spectral line profile were obtained, giving the electric field or the transverse velocity distribution as a function of time in a single discharge.

[a]Present address: Southwest Inst. of Nuclear Physics and Chemistry, P.O. Box 515, Chengdu, China.
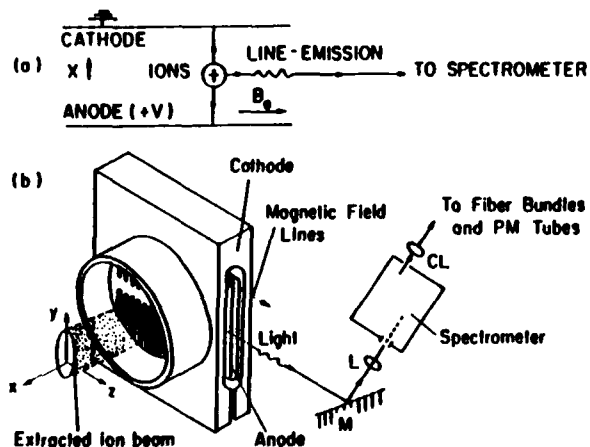
Fig. 1. (a) Method for measuring the electric field E in the acceleration gap of a magnetically insulated diode. (b) Schematic illustration of the planar magnetically insulated diode and the optical arrangement. The distance of the observation region from the anode is varied by moving the mirror M in the x direction.

Measurements of the electric field

The profile of the unshifted 4529 Å Al^{++} emission from the anode plasma, and the red shifted emission from the gap are shown in Fig. 2. The signal from the gap at the zero-field wavelength (i.e., the signal in the fiber bundle centered at 4529.2 Å) was determined to be due to the scattering of the unshifted intense plasma light. Therefore, it was ignored when the ion emission from the gap was analyzed to give the electric field.
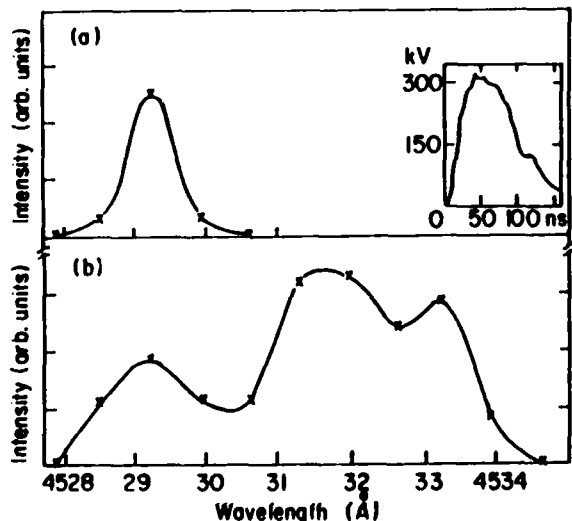

Fig. 2. (a) Spectral profile of the $4d_{5/2} \to 4p_{3/2}$ Al^{++} emission from the anode plasma: $x=0.15$ cm and $t=70$ ns. The zero-field wavelength is 4529.2 Å. The initial A-K gap $d_o=0.65$ cm and B=8.4 kG. The inductively corrected dioae voltage, monitored by a capacitive probe is shown in the insert. (b) Spectral profile from the acceleration gap at $x=0.375$ cm and $t=65$ ns. The line indicates the trend.

To determine the electric field, we calculated the theoretical emission profiles along the magnetic field from an ion in the presence of perpendicular electric E_x and magnetic B_x fields, for the known B_x and a range of possible E_x. The electric field was then inferred from a least squares fit of the calculated pattern to the measured points of the emission spectral distribution. Since this analysis assumed a single value of the electric field, it gives, for each position x, the mean electric field E over a plane parallel to the anode.

Figure 3 shows examples of measured $E(x)$ profiles for two diode configurations, one with a planar cathode and the other with a vaned cathode. In the latter, a 14-cm-long thin stainless-steel vane was connected to the cathode, parallel to the magnetic field lines projecting 3.5 mm into the gap opposite the top of the dielectric-anode (the electrons E×B drifted downward). The measured $E(x)$ profiles were used to infer the instantaneous actual diode gap with an uncertainty of ±0.075 cm. As seen in Fig. 3, the field-excluding anode plasma expanded about 3 mm away from the solid anode surface during the first 35 ns of the pulse, implying a plasma expansion velocity of 5-15 cm/µs. This decrease of the diode gap results in
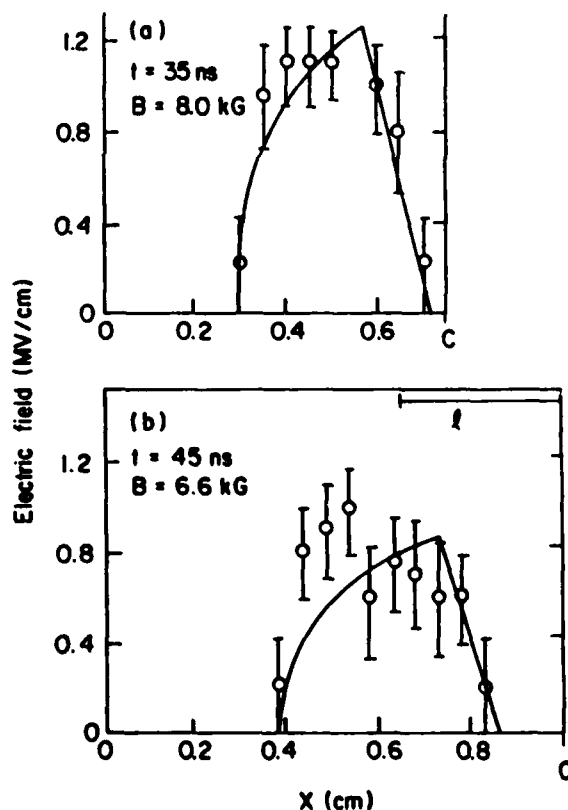

Fig. 3. a) Measured electric field distribution $E(x)$ for a planar diode configuration with $d_o=0.75$. The solid anode surface is at $x=0$ and the cathode surface is indicated by the C. b) $E(x)$ for a vaned cathode configuration with $d_o=1$ cm; the vane length l was 3.5mm. The lines are calculated [4] $E(x)$ profiles using the actual gap.

an increase of a factor of 2-4 in the space-charge-limited ion current density over the value calculated using the mechanical (initially set) diode gap.

We have used the actual diode gap to compare our $E(x)$ profiles to calculations based on the brillouin-flow model [4]. Such a comparison (see Fig. 3), when done for many shots, shows a trend: the measured electric field is higher than the calculated one in the region close to the anode. This trend, which is more pronounced for the vaned-cathode configuration, implies electron presence beyond the theoretical [4,7] electron-sheath region.

Analysis of Diode Space Charge

A detailed description of the electron density distribution and its implications inferred from our measured $E(x)$, will be given elsewhere [8]. To summarize, we obtain the potential profile $\varphi(x)$ by $\varphi(x) = V - \int_o^x E(x)dx$, and the ion velocity:

$$v_i(x) = (2e(V - \varphi(x))/m_i)^{1/2}, \qquad (1)$$

where e is the ion charge, m_i is the ion mass, V is the instantaneous diode voltage, and $v_i(0)=0$. The ion current density J_i, measured by a Faraday cup, is used then to give the ion density $n_i(x) = J_i/ev_i(x)$. We define the total electron number $N_e(x) = \int_x^{x_c} n_e(x)dx$ per cm^2 between the cathode plasma boundary x_c and a position x in the gap. From Poisson's equation, it is given by

$$N_e(x) = 5.53 \cdot 10^{11} E(x) + N_i(x), \qquad (2)$$

where $N_i(x)$ is the total ion number per cm^2 between x_c and x, and $E(x)$ is expressed in MV/cm. Using Eq. 2 we infer the total electron population N_g per cm^2 in the diode gap. We then use the model of ref. 4 to calculate (using the actual gap) the theoretical thickness s of the electron-sheath, the theoretical ion current density J_{ith}, and the total electron number N_{ths} per cm^2 in the sheath. In addition, we obtain (using Eq. 2) the experimental electron number N_{es} per cm^2 in a slab of thickness s adjacent to the cathode plasma.

For the vaned cathode configuration we found that N_g/N_{ths} and N_g/N_{es} are ~2. Assuming space-charge-limited flow one would anticipate from this that the ion current density would exceed the calculated [4] one. Indeed, for this configuration, we observed J_i/J_{ith} between 2 and 6. The uncertainty is dominated by the uncertainty in the inferred d, which again illustrates the need to know the actual diode gap in order to understand the operation of high-power diodes. We note that in this analysis we assumed J_i was uniform over the entire anode. The enhanced electron presence near the anode for the vaned-cathode configuration presumably results from the vane tip's emitting electrons which approach the anode and ExB drift in front of it over most of its area.

Transverse Velocity Measurements

Figure 4 shows measured profiles of the C^{++} 4647 Å emission from the anode plasma and from the diode gap. The Zeeman splitting for this line is ~0.2 Å and its Stark shift under our electric field is <0.1 Å. Thus the broadened line profile in the gap gives the distribution of the C^{++} ion velocities parallel to the magnetic field. In Fig. 4 we plot, for example, a Gaussian fit to the data. However, to estimate the uncertainty resulting from the unknown line-shape, we have analyzed our data assuming Gaussian and Lorentzian profiles. Including the measurement error we obtain that 50% of the C^{++} ions have transverse velocities less than $(4 \pm 1.5)cm/\mu s$. Using the ion axial velocity at the measurement axial position, $185 cm/\mu s$ (from Eq. 1), we conclude that the divergence angle of 50% of the C^{++} ions is less than $(1.4° \pm 0.5°)$ in the direction parallel to B at the x position of the measurement.

Using the 3602 Å Al^{++} line we found similarly that 50% of the Al^{++} ions have transverse velocities less than $(3.4 \pm 1.0)cm/\mu s$, which corresponds to a divergence angle of less than $(1.6° \pm 0.5°)$, again at the x position of the measurement. We also compared best fits of the same function (Gaussian or Lorentzian) for the Al^{++} and the C^{++} data. This comparison suggests that the transverse velocities scale as $(e/m_i)^{1/2}$. However, transverse velocities not dependent on e/m_i was also consistent with the data. Since our measurements were made at a diode position at which the ions had reached 1/3 to 1/2 their full energy, if they do not gain additional transverse velocity before leaving the diode, their divergence angle at extraction would be about 2/3 of the values quoted above. These are to be compared with previous measurements [6] of the proton divergence angle outside the diode parallel to B which yielded 4-5°.
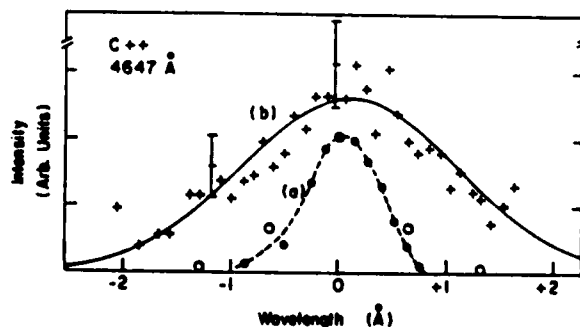

Fig. 4. The open circles constitute the spectral profile of the C^{++} 4647.4 Å line emission from the anode plasma ($x = 1$ mm, $t = 50$ ns). Curve (a) and the solid points give the system response. The emission from the gap ($x = 5.5$ mm) averaged over $t = 30 - 70$ ns is shown by + points and curve (b) is a Gaussian best fit.

Conclusions

The results described here from the electric field measurement, namely the rapid early time gap closure and the presence of substantial electron space charge near the anode, especially in diodes with cathode vanes, provide an explanation for the enhanced ion current density in magnetically insulated diodes operating at modest power densities such as ours. Taken together with the highly diamagnetic electron flow characteristic of high power density diodes, as discussed in ref. 9, our results may also explain the enhancements of 40 or more discussed by Miller [10] in experiments on Proto I, Proto II and PBFA I.

Finally, we note that if the diagnostic tool described here is used to obtain information about the charge flow and the ion transverse velocities in diodes with higher electric field, the Stark shift and the Doppler broadening (for a given divergence angle) will be larger. Moreover, with higher electric fields, there will be a higher ion current density, and lower-lying ionic energy levels will be sufficiently shifted to be useful, both of which will contribute to having more signal. Therefore, the measurements described here should be easier in diodes with higher electric fields than the one used here.

References

1. D.J. Johnson, E.J.T. Burns, J.P. Quintenz, K.W. Beig, A.V. Farnsworth, Jr., L.P. Mix and M.A. Palmer, J. Appl. Phys. **52**, 168 (1981).

2. J.E. Maenchen, F.C. Young, R. Stringfield, S.J. Stephanakis, D. Mosher, Shyke A. Goldstein, R.D. Genuario and G. Cooperstein, J. Appl. Phys. **54**, 89 (1983).

3. R. Pal and D.A. Hammer, Phys. Rev. Lett. **50**, 732 (1983).

4. T.M. Antonsen and E. Ott, Phys. Fluids, **19**, 52 (1976).

5. Y. Maron and C. Litwin, J. Appl. Phys. **54**, 2086 (1983).

6. J. Maenchen, L. Wiley, S. Humphries, Jr., E. Peleg, R.N. Sudan and D.A. Hammer, Phys. Fluids **22**, 555 (1979).

7. R.N. Sudan and R.V. Lovelace, Phys. Rev. Lett. **31**, 1174 (1973).

8. Y. Maron, M.D. Coleman, D.A. Hammer, and H.-S. Peng, in preparation.

9. S.A. Slutz, D.B. Seidel and R.S. Coats, J. Appl. Phys. **59**, 11 (1986).

10. P.A. Miller, J. Appl. Phys. **57**, 1473 (1985).

HIGH GRADIENT ELECTRON ACCELERATORS USING FAST WAVES ON BEAMS

John A. Nation and S. Greenwald
Laboratory of Plasma Studies and School of Electrical Engineering
Cornell University, Ithaca, NY 14853

A novel technique for the production of medium or high energy electron beams from a high current, sub megavolt pulse power drive electron beam is described.

A high current weakly relativistic electron beam is used to excite high power microwave radiation in a transverse magnetic mode. The microwave radiation is propagated through an undulating guide which serves to couple the fast electromagnetic wave to the electrons. The period of the undulation is chosen such that the electrons slip one cycle of the rf wave every period of the undulation. The process envisioned, which produces a continuous acceleration of the electrons, is similar to that proposed in the Inverse Free Electron Laser accelerator [1]. Examples are presented showing the trade off between the average acceleration electric field gradient and the average beam current.

Introduction

We examine in this paper a novel technique for the acceleration of electrons to medium or high energies. The proposed technique uses a high current weakly relativistic electron beam to generate a high power microwave signal in a transverse magnetic mode of the guide. These processes have been developed over the last decade [2, 3] and have been shown to be capable of producing gigawatt power pulses at frequencies in excess of 10 GHz. The efficiency of the microwave generation approaches 20%. The radiation is then used to accelerate a lower current secondary beam of electrons to high energy. The acceleration occurs in a smooth bore undulating waveguide with the electrons slipping one cycle of the rf wave every period of the undulation. By use of the TM02 mode (or a higher order mode) we can use the phase slip to advantage so that, as the electrons sample the different radial positions of the guide, the axial electric field is always in the sense leading to acceleration. It is worth noting certain features of this accelerator concept. Pulse power sources are used to generate short pulses (~ 50-100 nsec.) of high power microwave radiation. In order to couple these effectively to a secondary beam for acceleration it is necessary to use a coupling structure with a moderately high group velocity. In the proposed accelerator the velocity is typically of order 0.4c, a value substantially larger than that encountered in conventional r.f. linacs. Other interesting and desirable features include:

i. The use of overmoded guide so that higher frequencies can be used relatively easily.

ii. The electric field peaks on axis and not at the boundaries of the structure. This reduces the possibility of breakdown at guide boundaries.

iii. The absence of transverse cavities reduces the possibility of beam break-up as a result of the excitation of unwanted cavity modes. This latter feature should permit the use of larger beam currents without serious instability.

iv. Wake field effects should not be any worse than those encountered in conventional slow wave structures and may be better at a fixed frequency since we operate in a high order guide mode. Wall proximity effects should therefore be reduced.

We now describe the accelerator concept in detail. Low average current beams may be accelerated to very high energies at gradients in excess of 100 MV/m or, by allowing a reduction in the achievable gradient, we can accelerate beams with average currents of order of a few hundred amperes at field gradients of order 10 MV/m. The former accelerator configuration is of interest for high energy physics applications while the lower gradient, high current, device may be used for a variety of applications including the driving of free electron lasers.

Accelerator Concept

We consider an electromagnetic wave propagating through an undulating guide. The undulation period is Γ and its amplitude r_o. The

axis of the guide varies sinusoidally as a function of position according to

$$r(z) = r_0 \sin(2\pi z/\Gamma) \qquad (1)$$

The electron beam propagates through the guide parallel to the z axis with a velocity $v \approx c$. For simplicity we take $r_0/\Gamma \ll 1$. The force felt by an electron due to the rf wave is

$$F(z) = eE_0 J_0[k_c r_0 \sin(2\pi z/\Gamma)]\cos(\omega t - kz) \qquad (2)$$

and averages to zero unless the synchronism condition

$$\beta_e = \frac{\omega}{(k + 2nK)c} \qquad (3)$$

applies, where k and K are the wavenumbers of the wave and the ripple respectively, ω the wave frequency, β_e the normalized electron velocity, c the speed of light and n an integer, which we shall assume to be unity in what follows. Using the synchronism condition Eq. 2 becomes

$$F(z) = eE_0 J_0[k_c r_0 \sin(2\pi z/\Gamma)]\cos(4\pi z/\Gamma) \qquad (4)$$

At z = 0, $\Gamma/2$, and Γ the electrons feel the full axial field E_0 of the TM wave. Mid way between these points, the electrons are located close to the second radial extremum of the axial electric field of the TM mode. The field gradient is shown as a function of axial position in Fig. 1.
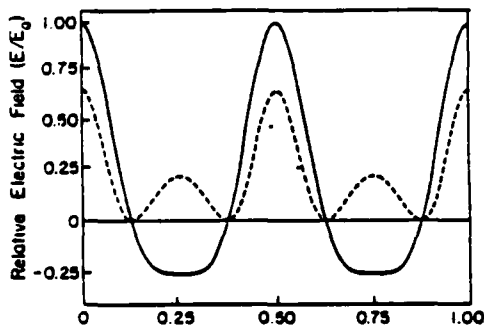
Fig. 1.

Relative electric field felt by an electron as a function of position in the undulator. The electric field is normalized to that on axis in the TM01 mode at the same power level and for a fixed ratio of the wave to the guide cut-off frequency. The solid line represents the TM01 mode with r/a = 0.8 and the dashed line the TM02 mode with r/a = 0.6.

Figure 2 shows the field gradient averaged over a period of the undulator for the TM02 mode at various power levels. The average
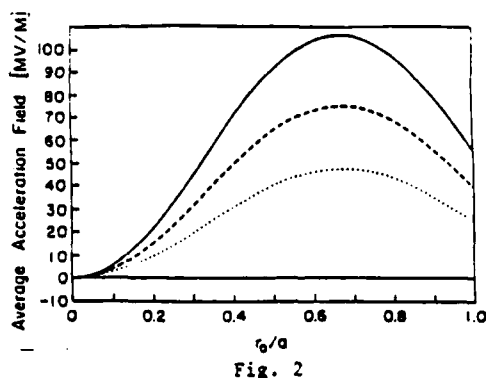
Fig. 2

Acceleration field averaged over the undulator period for a TM02 mode at 35 GHz as a function of r_0/a at power levels of 1 GW, 500 MW and 200 MW respectively.

field gradient achievable in the TM02 mode is higher than that achievable in the fundamental mode since an electron must lose energy in propagation through half the undulator period. The axial electric field in the TM modes increases rapidly as the wave frequency decreases towards the cut-off frequency for the mode. A practical limit is set on the operating frequency by the reduction in the wave group velocity on the one hand and the increase in the guide losses on the other. At a fixed value of the wave phase velocity the achievable field at fixed power through the guide varies proportionally with the wave frequency.

Acceleration in a Standing Wave

We consider the case of an undulating guide, which satisfies the criterion of Eq. 3 for wave-electron synchronism, as part of a cavity of length L >> Γ. The synchronism condition is identical to that given earlier with now, the wave number k = π p/L determined by the resonant frequency of the cavity and the cut-off frequency of the guide. Note that the synchronism condition may be expressed in the alternate form.

$$\Gamma = \lambda_G \frac{\beta_e}{\beta_\phi - \beta_e} \qquad (5)$$

where λ_G, is the guide wavelength and β_ϕ the wave phase velocity. This form is instructive since it shows that no special tuning of the guide undulation period is needed as the electron energy increases. At synchronism, the electric field felt by an electron in traversing a period of the undulator in the cavity is given by

$$E(z) = E_{ax} J_0 (k_c r_0 \sin(\frac{2\pi z}{\Gamma})) \cos(\frac{\pi p z}{L})$$

$$\cos[(k + 2K)z] \qquad (6)$$
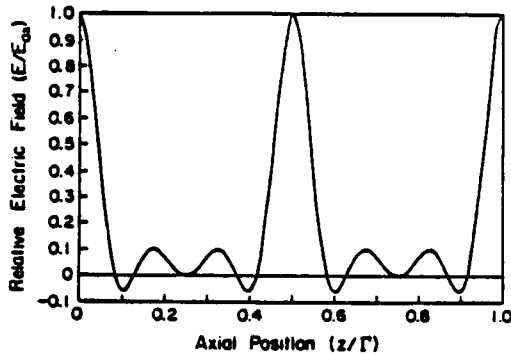
This result is plotted out in Fig. 3.

Fig. 3

Local acceleration field normalized to the peak electric field on axis. The cavity is excited by a TM02 mode at 35 GHz. The cavity length is 1m (p = 78) and r_0/a = 0.6. The guide wavelength has been chosen to be equal to the undulator period.

In Fig. 4 we show the acceleration field achievable, averaged over the undulator period. The field gradient is shown as a function of the non-dimensional curvature (r_0/a) of the guide. The axial field strength was determined by equating the power losses in the walls (assuming copper walls are room temperature) to the power in from the source. Input power levels of 100 and 500 MW were assumed.
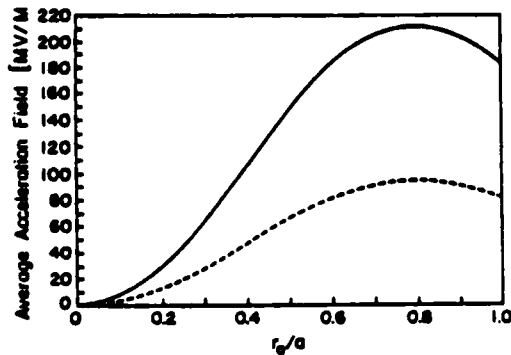

Fig. 4

Average acceleration field calculated for 100 and 500 MW at 35 GHz.

Note that for the 1 m cavity length assumed, the wave energy transit time, L/v_g, is only 10 nsec. The average field gradients achieved in this case are comparable to those shown in Fig. 2 but

with power levels about one order of magnitude lower. An interesting variant on the cavity which combines the advantages of the cavity mode of operation yet retains the desirable features of the travelling wave accelerator is the travelling wave resonator proposed in the fifties [4]. In this configuration, a single wave circulates around a racetrack with the resonance condition being set by the cavity length being an integral number of guide wavelengths. In this case the ratio of the acceleration field to the axial field is the same as in the travelling wave case.

Accelerator Parameters

We present in this section typical accelerators parameters for two applications, namely a high energy electron accelerator and secondly, a high average current device at medium energy. Table 1 shows the operating parameters for a high energy accelerator operated in the travelling wave TM02 mode at 35 GHz, and in the cavity mode at 12.5 GHz. The wave to cut-off frequency is 1.06 corresponding to a wave group velocity of 0.33c. The travelling wave module length is 6 m and the cavity module length 1 m. We assume that the cavity is pumped for one quarter of the filling time 2Q/ω at the specified power level and it is assumed that the beam drains the stored energy completely. The average beam current is computed on the basis of a repetition rate of 1 kHz and the peak current on the basis of allowing a 1.5% spread in the output beam energy.

Table I.

	TM_{02} Travelling Wave	TM_{02} Cavity Mode
Frequency (GHz)	35	12.5
Power (MW)	1000	500
Field on Axis (MV/m)	310	450
Acceleration Field (MV/m)	100	100
Undulator Period (cm)	2.8	7.2
Wall Modulation	0.6	0.6
Number of Particles/ Bunch	4×10^{11}	3×10^{12}
Average Current (μA)	64	500
Synchrotron Radiation Energy Loss (MeV/m at 100 GeV)	0.8	2

Synchrotron radiation losses have been estimated for this device and are tabulated. The losses arise from the radial forces. Since the primary acceleration field is axial the radiation losses are minimal and are unimportant until energies of order 1 TeV are achieved. The losses scale as the axial field squared.

In Table II we show a case representing the generation of an high average current modulated beam suitable for use, for example, in an FEL experiment. Once again, we assume a module length of 1 m. In this case, the output beam consists of a train of closely spaced bunches each of which is of very short duration and are separated from each other by the wave transit time through the cavity (~ 10 nsec.). In the example given the beam has an average current of 100 A, a peak current of 1.8 kA, and an energy spread of about 1%.

Table II.

Frequency (GHz)	5.7
Power (GW)	1.0
Field on Axis (MV/m)	50
Acceleration Field (MV/m)	10
Undulator Period (cm)	17
Wall Modulation	0.3
Number of Particles/Bunch	1.5×10^{11}
Max Bunch Rate (sec^{-1})	4×10^{9}
Peak Current (kA)	1.8
Average Current (A)	100

Concluding Comments

We conclude this paper with some comments regarding possible limitations in the proposed accelerator. One concern is that the wave propagation will be very different to that assumed. It is clear that we have a periodic structure and that this will result in a modification of the expected uniform guide modes. To examine this we have fabricated a 60 cm long test section of 2.5 cm radius guide with $r_o/a = 0.5$ and $\Gamma = 16$ cm. Preliminary test results are given in Fig. 5 which shows propagation in the TM11 mode from 4 to 14 GHz.

A detailed analysis of the network analyzer output yields a dispersion relationship similar to that obtained in a section of uniform pipe. There exists an upward shift in the frequency of up to 500 MHz which we attribute to distortion in the guide cross section during the bending process. Our qualitative expectations that the dispersion would not change significantly if Γ
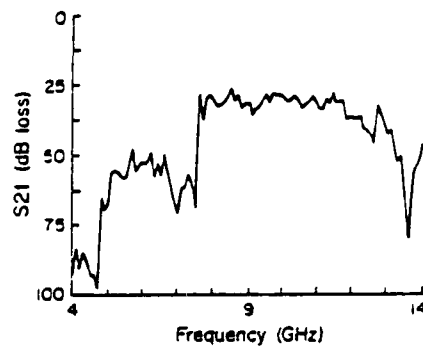

Fig. 5

Propagation in the TM11 mode through a 60 cm long undulator guide, with $r_o/a = 0.5$, as a function of frequency.

$>> \lambda_g$ appear to be substantiated. We also have results showing propagation in the TM02 mode with no noticeable mode conversion. This case is more difficult to test experimentally as we still excite some TM01 mode simultaneously with the TM02 mode. In any event we find, even with quite severe curvature of the guide, that the uniform guide mode is essentially preserved.

We conclude that the proposed accelerator configurations show promise for use of giant power microwave pulses in electron accelerators. The final success of this proposed accelerator probably depends on the achievable phase stability of the sources.

References

1. C. Pellegrini, American Institute of Physics Conf. Proc. 91, 138, (1982).

2. N. F. Kovalev, M. I. Petelin, M. D. Raizer, A. V. Smorgonskii, and L. E. Tsopp, JETP Lett., 18, 138, (1973)

3. Y. Carmel, J. Ivers, R. E. Kriabel, and J. A. Nation, Phys. Rev. Lett., 33, 1278, (1974).

4. F. J. Tischer, Institute of Radio Engineers Trans. on Microwave Theory and Techniques, 51, (1957).

ION DIODE EXPERIMENTS AT THE 0.5 TW LEVEL ON THE LION ACCELERATOR*

G.D. Rondeau, C. Peugnet**, J.B. Greenly, D.A. Hammer,
B.R. Kusse, E. Pampellonne, and R.N. Sudan

Laboratory of Plasma Studies,
Cornell University,
Ithaca, N.Y. 14853

Abstract

Light ion inertial confinement fusion
research at Cornell includes two ion diode
development experiments which utilize the 0.8TW
(1.8MV, 450kA), 40ns LION accelerator. One
uses a B_r extraction geometry magnetically
insulated diode and has two goals: to study ion
beam generation using an exploding metal film
anode plasma source, and to study ion beam
propagation and focussing. The second experiment
utilizes the B_z "barrel" geometry and its goals
are: to determine if this symmetric diode can be
run on a "single sided" generator, and, if so, to
investigate the effects on diode operation of
pulse risetime, the details of the magnetic field
geometry, and other mechanisms that affect
electron leakage to the anode. Results from
these experiments are described.

Introduction

In this paper, we report research progress
at Cornell University since the last beams con-
ference [1] on the generation of intense ion
beams for inertial confinement fusion (ICF). Our
effort involves two ion diode development
experiments using the 0.8TW (1.8MV, 450 kA), 40
ns LION accelerator, a module of the PBFA I
machine. One experiment utilizes an extraction
geometry magnetically insulated diode (MID) and
has two goals, the development of an exploding
metal film active anode plasma source (EMFAAPS),
and the study of the propagation and focussing of
an intense ion beam from an extraction diode.
The EMFAAPS is driven by the first few nano-
seconds of the LION power pulse via a plasma
opening switch. Using aluminum foils, about
500A/cm^2 of ions heavier than protons (and
200A/cm^2 of protons) have been produced at about
1MeV. Propagation and focussing experiments have
so far been performed only with an epoxy-filled
"surface flashover" anode in place of EMFAAPS.
Preliminary results show a radial aiming error
that may be due to a small electric field (about
10kV/cm) in the strong transverse magnetic field

region near the diode insulation coils, or to the
virtual cathode being tilted with respect to the
anode surface.

The second experiment utilizes the applied
B_z barrel MID configuration of Johnson et al.
[2]. The first goal of this experiment was to
determine if this cylindrically symmetric diode,
which is also symmetric about its midplane, can
be efficiently operated using a power source
(LION) which is not inherently symmetric about
the diode midplane. Recent results in which
reasonably uniform ion beams have been produced
suggest that this can be done. We are now
characterizing the operation of the diode and the
ion beam it produces under "standard conditions".
We will then investigate the effects on diode
operation of pulse rise time and mechanisms which
affect the electron leakage to the anode (e.g. -
an electron limiter [3], azimuthal asymmetries,
and the overall magnetic field geometry).

Extractor Diode Experiments

EMFAAPS

The development of an adequate anode plasma
ion source for light ion ICF is a high priority
problem at the ignition experiment level. We are
investigating an exploding metal film active
anode plasma source (EMFAAPS). We have found
that a metal film deposited on a plastic surface
can be made to explode with reasonable
uniformity, as determined from the visible light
image using a streak camera, when driven by the
first few nanoseconds of the LION accelerator
power pulse [4]. This technique has now been
tested using an evaporated metal film (500 Å of
aluminum) on an epoxy anode mounted in the diode
shown in Fig. 1. The film is vaporized and
undergoes electrical breakdown by passing the
generator current through the film via the plasma
switch shown inside the anode in Fig. 1. High
voltage appears across the anode-cathode gap as
the plasma switch impedance rises, allowing a
high current ion beam to be extracted. The

plasma switch geometry used here does not open; instead the switch current remains nearly constant at 80 - 150A (depending on the precise plasma switch conditions) during the high voltage phase of the pulse, (see dashed trace in Fig 2b).

The earliest tests with EMFAAPS produced very low impedance diode operation and a great deal of electron damage to the inner portions of the anode, even though $B/B^* >1.8$, where B^* is the critical field for magnetic insulation [5]. Field mapping showed flux surfaces crossing the epoxy anode surface at the location of the damage. The epoxy thickness was modified to eliminate the intersections of flux surfaces and the epoxy surface resulting in the diode electrode and flux surface configurations shown in Fig. 3. The result was decreased electron damage, and higher impedance diode operation, as shown in Fig. 2. In this shot, peak voltage was about 1 MV and peak total current was about 400 kA. Of that total, about 150kA is switch current, 150 kA (peak) is ion current and the remainder is electron leakage current.

Also shown in Fig.2 are three Faraday cup traces from cups located 9 and 14 cm from the anode. Two current peaks are visible. The first is consistent with prompt turn-on of the anode if the time-of-flight of protons is taken into account. The second is consistent with prompt anode turn-on and time-of-flight for Al^+. The proton contamination is to be expected since no effort was made to avoid it. Thus, although we have not confirmed that the heavier species is Al^+, we believe that we are seeing a peak current density of 400-700 A/cm^2 of that species a distance of 9 cm from the anode. Since the area of the anode is about 160 cm^2, we estimate a total peak Al^+ current of (90 ± 30) kA. Because of the time of flight spreading of the beam in propagating to the Faraday cups, this may be an underestimate. The proton peak current density of 250-400 A/cm^2 similarly extrapolates to a total peak proton current of (50 ± 10) kA. However, notice that the proton peak is only about 15 ns wide, suggesting that the proton component in the anode plasma is depleted in the first few ns of the power pulse using EMFAAPS.

After each shot, the aluminum film is completely gone and, in the less damaging pulses, electron damage is confined to a small region of the epoxy substrate near the inside radius of the anode.

Ion Beam Propagation and Focussing Experiments

The diode shown in Fig. 1 has also been used with a more conventional epoxy-filled-groove aluminum anode instead of the EMFAAPS to extract an ion beam and study its propagation and focussing. Measurements of the mean direction of motion and the intrinsic divergence of a portion of the ion beam have been made by placing a pinhole aperture 9 cm from the anode (just behind the cathode flange in the field free drift space, see Fig. 1). The selected beamlet is then incident on an array of charge collectors, the geometry of which is shown in Fig. 1. Because of the short (50 ns) diode power pulse and the nearly 20 ns turn-on delay with epoxy-filled-groove anodes, time-of-flight separation allows the unfolding of direction-of-motion information for the various ion species in the beam, and divergence information for the protons.

Figure 4 shows data from a shot with the aperture located near the outer edged of the beam envelope. Ions began to appear at about 30 ns and the peak of the ion power pulse was at about 53 ns on this shot. At that time the proton divergence is about 3 degrees FWHM. The peaks for ions heavier than protons, assumed to be C^+ and C^{++}, overlap for much of the pulse so determining the divergence for these ions is not possible. During the pulse, the ratio of C^{++} to C^+ seems to increase although again because of the overlap it is difficult to quantify the ratio. The proton and the C^{++} peaks move rapidly inward with time. Figure 5 shows a comparison of the observed deflection of the ions with a calculated deflection that accounts for magnetic bending but assumes there is no space charge electric field (i.e. - the beam is fully charge neutralized). The calculation assumes that ions leave the anode normal to the surface with an energy determined by the instantaneous value of the voltage, that the beam current is neutralized once it passes through the entrance of the flux conserving cathode extraction flange, and that canonical angular momentum is conserved. The actual deflection of the proton component of the beam is consistently 2-4 degrees less than the calculated values. Figure 5 also shows the measured and calculated deflection for C^+ ions, which are not as affected by the magnetic fields. If we estimate the space charge electric field required to deflect the ions by 1.5° assuming it is

present uniformly whereever there is strong magnetic field, we find that a field of about 10 kV/cm is enough. This corresponds to > 99.9% charge neutrality of the ion beam. Although the C^{++} ion mean deflection angle was also obtained, and the results regarding a space charge electric field obtained with them is consistent with the above discussion, we do not include them in Fig. 5 in order to avoid overly complicating it.

Another possible source of the observed outward deflection of the ions is a virtual cathode which is not parallel to the anode surface. This might result from the inherent 1/r dependence of the insulating magnetic field. If the virtual cathode is tilted and the ion current density is space charge limited, then the ion current density should give an indication of the variation of the effective gap spacing d through the $1/d^2$ current density dependence. Figure 6 shows signals from three Faraday cups radially separated by 0.8 cm, placed immediately behind the cathode. Notice that the highest current density is seen by the outer cup, the middle one is next, and the inner one is lowest. Figure 6 also shows the values of d obtained using the space charge limited current density formula, with the instantaneous voltage taken from the upper trace in the figure. The difference in d implied by the detectors taken in pairs divided by the spacing between them gives an angle (in radians) which may be interpreted as the angle of the virtual cathode with respect to the anode surface. This angle is shown in degrees in the bottom graph in Fig. 6. Since the curves are constructed from the difference between two noisy signals, the details of the two curves are probably not significant. However, the general trend of this angle would imply an outward deflection of the ions early in time which would gradually decrease to no deflection at the end of the pulse, as seen for the carbon ions (Fig. 5).

B Diode experiments

The B_z diode used here (see Fig 7) is a replica of the Proto I ion diode used by D.J. Johnson et al. [2] at Sandia but modified as needed to be used on the LION accelerator. The cathode is made of aluminum and is a flux excluder. In contrast to multimodule pulsed power generators such as Proto I and the PBFA I

and II halves of the B_z diode symmetrically, here we must provide paths to the two sides of the diode so as to balance the current flow from LION. The geometry shown in Fig. 7 is designed to have equal inductances for the two current paths. Experiments presently in progress have determined that it is possible to balance the feeds and generate a uniform ion beam at a diode voltage up to about 1 MV. Figure 8 shows a sample set of data from a shot in which a damage target showed that a reasonably uniform ion beam was produced. On this shot the peak inner and outer currents, I_1, and I_2, were 110kA and 120kA respectively, with an incident current of 260kA. Leakage current at the post-hole convolute was measured to be < 5% of the incident current.

At the present time we are developing techniques to characterize diode operation and ion beam quality, and we will shortly undertake the following:

(1). Investigate the effect on the turn-on delay of an epoxy-filled-groove flashover anode as the pusle rise time is varied with a plasma opening switch.

(2). With a gas cell installed in the volume inside the cathode, study the current neutralization phenomenon in detail.

(3). Determine the effect of anode geometry and magnetic diffusion into the anode on the ion focussing.

(1). D.A. Hammer, B.R. Kusse, J. Maenchen, A. Manofsky, J. Neri, T.J. Renk and R.N. Sudan, in Proc. Fifth Int. Conf. On High-Power Particle Beams, R.J. Briggs and A.J. Toepfer, Eds., (San Francisco, 1983), p 56.
(2) D.J. Johnson, R.J. Leeper, W.A. Stygar, R.S. Coats, T.A. Mehlhorn, J.P. Quintenz, S.A. Slutz, and M.A. Sweeney, J. Appl. Phys. 58, 12 (1985).
(3) S.A. Slutz, Private Communisation
(4) G.D. Rondeau, J. Aborn, J.B. Greenly, D.A. Hammer and B.R. Kusse, Cornell University Report LPS 345, October 1985.
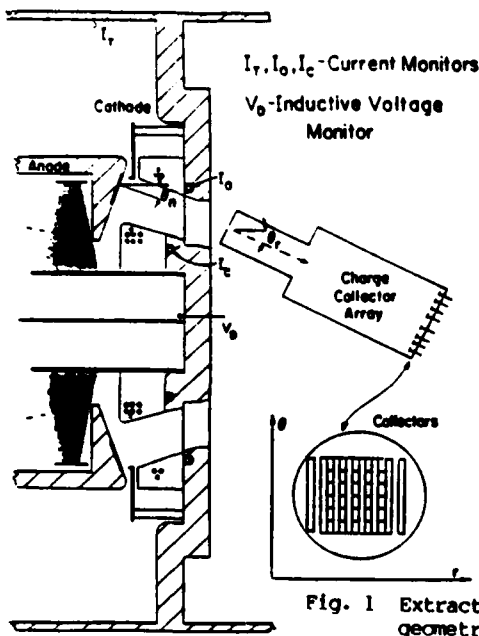(5) R.N. Sudan and R.V. Lovelace, Phys. Rev. Lett. 31, 1174 (1973).

I_T, I_O, I_C-Current Monitors

V_D-Inductive Voltage Monitor

Fig. 1 Extraction geometry diode.

EMFAAPS DATA

(a) 800 kV

(b) 300 kA
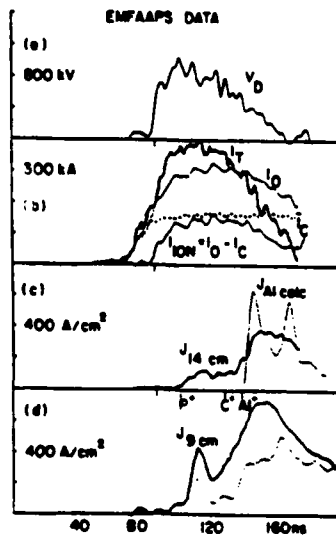
(c) 400 A/cm²

(d) 400 A/cm²

Fig. 2 EMFAAPS shot data. (a) V_d (b) I_T I_o I_c and I_{Ion} (c) observed and calculated (light curve) current densities 14 cm from anode. (d) current density at two radial positions 9 cm from anode.
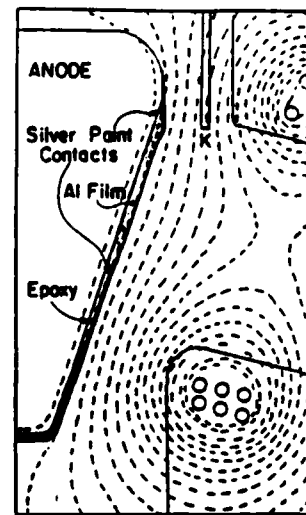

Fig. 3 EMFAAPS detailed configuration.

Fig. 4 Angle $\theta_r - \theta_n$

ION DEFLECTION VS TIME

○ PROTONS
● CARBON +
— CALCULATED

Fig. 5

1.6 MV VOLTAGE

1.2 kA/cm² Faraday Cups

Effective Gap

1.0 cm actual gap

Deflection

10°

Fig. 6

A Anode
B B field coils
C Post hole convolute (I of 6)
K Cathode tip
P Plasma switch region
S Flashboard plasma source
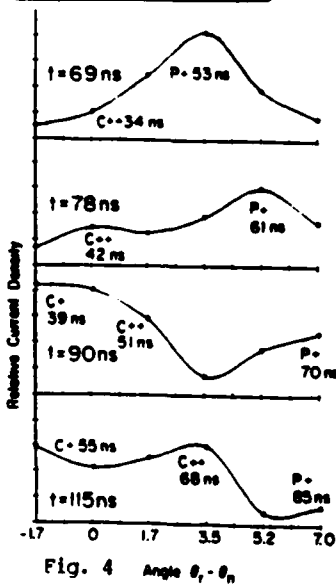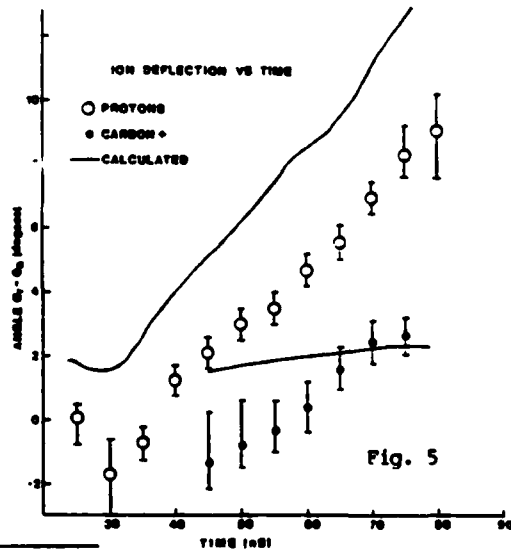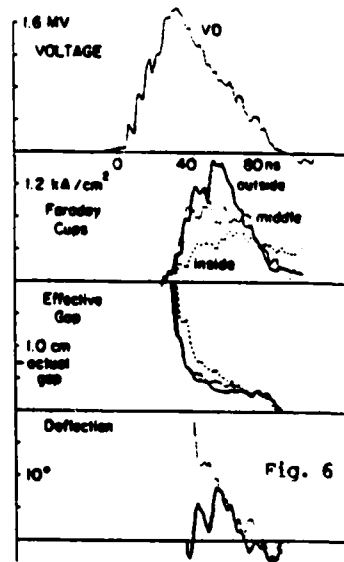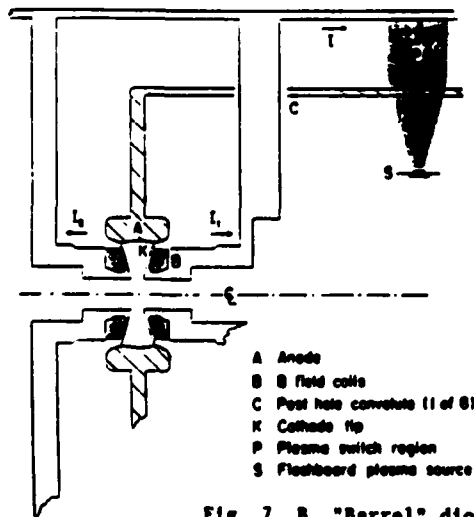
Fig. 7 B_z "Barrel" diode.
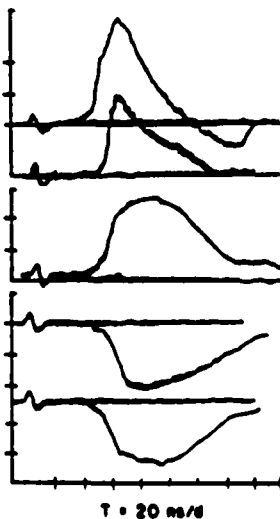
V_r = 450 kV/d

Xray diode

I = 95 kA/d

I_t = 49 kA/d

I_2 = 50 kA/d

Fig. 8 B_z diode data.

V_r is interface voltage

T = 20 ns/d

A HIGH CURRENT TWO STAGE INDUCTION LINAC

I. S. Roth, J. D. Ivers, and J. A. Nation
Laboratory of Plasma Studies and School of Electrical Engineering
Cornell University, Ithaca, NY 14853

Abstract

A two stage proton induction linac has been fabricated and the beam characteristics measured. The injected beam has an energy of 1 MeV with an ion current of up to 6.0 kA. The post acceleration gap increments the energy by 350 keV.

In this paper, we shall review the generation and transport of the proton beam through the accelerator. Time resolved ion profiles will be presented. The dynamics of the ion beam will be reviewed and examined. Time integrated proton flux and divergence measurements will also be presented as a function of position throughout the accelerator.

We shall also review the possibility of using space charge neutralized ion beams in multistage accelerators.

Introduction

We consider in this paper the use of linear induction accelerators for the production of high current, multi-megavolt ion beams [1,2,3]. For beam currents of several kilo-Amperes the self electric field of the beam is of order 50 MV/m and cannot be confined by modest (~1 Tesla) magnetic fields. In this experiment we present data on the design and performance of a two stage, 6 kA, proton induction linac. The ion beam, which is magnetically confined, is space charge neutralized by co-drifting electrons originating from the electron cloud defining the cathode plane. Additional neutralization is provided by electrons emitted from the drift tube wall.

Beam Parameters

The two stage linear induction accelerator has an inductively driven first stage which gives an injection energy of 1 MeV and a second stage post-acceleration of 350 kV; the half width of the pulse is 60 ns. Proton currents of up to 6 kA have been produced. The beam, which is generated in a magnetically insulated diode, is propagated in a solenoidal magnetic field to a cusp magnetic insulating field, where the post acceleration occurs. The experimental configuration is illustrated in Fig. 1.

Beam Diagnostics

Measurements were made of the ion and net current densities using radial arrays of Faraday cups. In order to measure the ion current density, the electrons co-drifting in the beam must be separated out. This is accomplished by the detector illustrated in Fig. 2. The axial magnetic field which confines the beam is excluded from the aperture in an iron plate. The beam electrons follow the field lines away from the aperture while the ions pass through the aperture to the collector. As a check on the per-
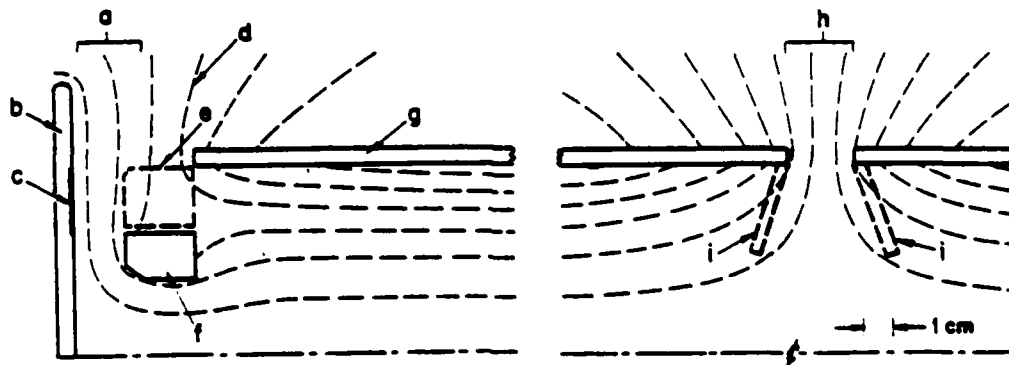

Fig. 1. Experimental configuration: (a) first acceleration gap, (b) anode, (c) proton emission surface, (d) electron emission fins, (e) field coil, (f) solenoid, (g) magnetic field lines, (h) second acceleration gap, (i) fins.
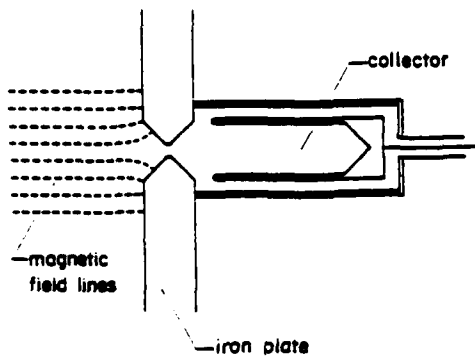
Fig. 2. Ion Faraday collector. The magnetic field lines are only shown entering the iron plate.

formance of the detector, the time integrated signal was compared with a carbon activation measurement. The Faraday cup signal was 59 ± 8 % of the carbon signal. This difference is primarily attributed to secondary electrons emitted from the inside surface of the aperture and collected by the cup.

The net current Faraday cup differs from the ion collecting cup in that the front aperture plate is brass and does not limit electron flow to the cup.

Carbon activation was used to measure the beam fluence over areas large compared to the 1.6 mm aperture of the Faraday cups.

Experimental Results

Beam Transport

Carbon activation measurements of the beam fluence are shown in Fig. 3 as a function of radius for several axial positions. The beam expands upon entry into the drift tube, and is in contact with the drift tube wall. The beam then detaches from the wall and moves inward, where it propagates with little further loss. The beam does not follow single particle trajectories, which have a calculated focal length of 35 cm. At a distance of 46 cm from the diode, the beam, while densest on axis, has only focussed to a mean radius of 3.3 cm from an average radius of 5.5 cm at injection.

Diodes, similar to that used in this work, typically produce ion beams with a mean divergence angle of about 3°. Measurements in this experiment indicate that the outermost protons expand radially at a 14° angle prior to entering the drift tube 2.5 cm downstream of the cathode plane. The subsequent radially inward proton motion indicates that the ion beam is neutral-
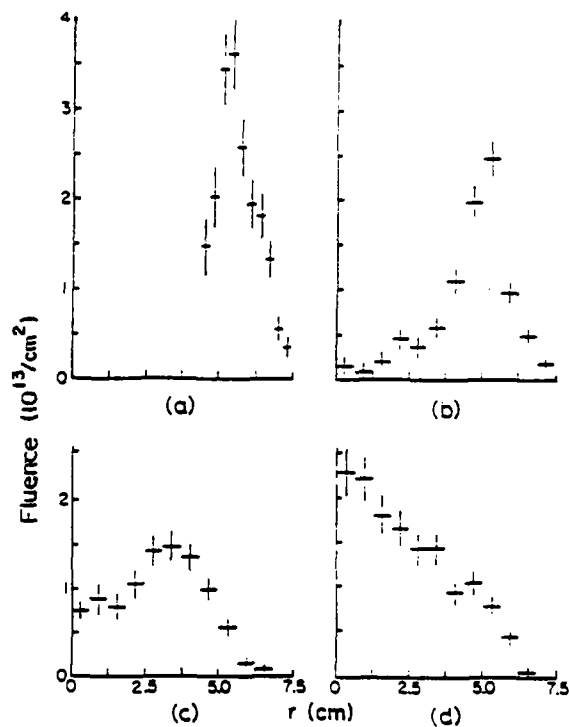
Fig. 3. Beam fluence as a function of radius at (a) 3 cm, (b) 17 cm, (c) 32 cm, and (d) 44 cm from cathode.

ized by electrons emitted from the drift tube wall. Approximately 20% of the diode generated beam is lost to the support struts for the inner magnetic field coil and a further 5% to the wall at the entrance to the drift tube. Following the beam detachment from the wall the transport through the first section of drift tube is 100% efficient.

A net current Faraday cup was used to sample the beam as a function of distance from the diode. The traces, shown in Fig. 4, indicate

Fig. 4. Net current density at 0.6 cm (a), 3.5 cm (b), 7.5 cm (c) and 12.5 cm (d) from cathode. The detector was at 5 cm radius.

Fig. 5. Ion current density at 1.2 and 3.5 cm radial positions for first (a) and (b) and subsequent shots (c) and (d).

that the net current density decreases from 40 to 5 A/cm^2 over the first 12.5 cm from the diode. This is consistent with the neutralizing electrons entering the beam along magnetic field lines at the entrance to the solenoid. (See Fig. 1).
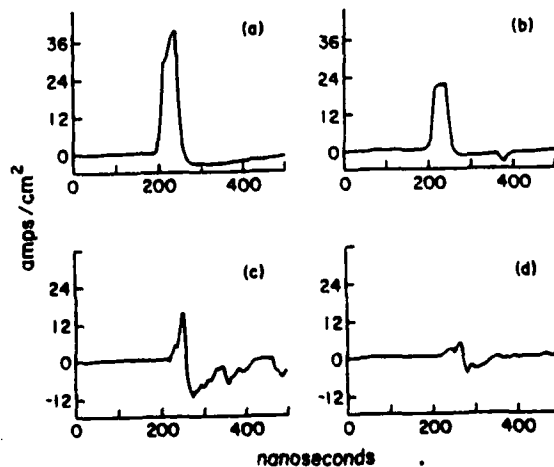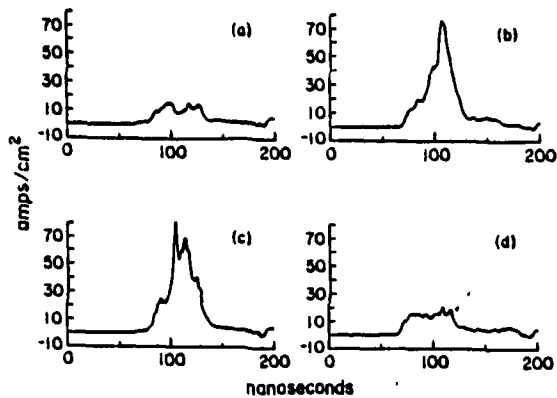
Additional confirmation of the importance of the walls in the space charge neutralization process was provided in a series of shots utilizing two iron aperture Faraday cups located at radii of 1.2 and 3.5 cm and at an axial location 30 cm downstream of the diode. Figure 5 shows the output from the two Faraday cups during a sequence of shots. The upper traces, taken on the first shot in the series, show peak ion current densities of 12 and 76 A/cm^2 on the inner and outer cups respectively. The second set of data, taken two shots later, show ion current densities at the cups of 80 and 20 A/cm^2 respectively. The current densities stabilized at the second set of values until the tube wall was cleaned, after which the signals returned to their earlier values. The gross difference in beam focussing seen here was due to additional beam space charge neutralization arising from the debris due to the blow off of dry silver copy paper, used in the experiment to generate an qualitative image of the time integrated beam profile. The effects of the wall contamination did however provide strong evidence for the importance of electron emission from the walls on the beam neutralization and dynamics, and might be used to advantage in the design of electron sources for space charge neutralization.

Data from Faraday cups can be used to form radial profiles of the current density. Pro-
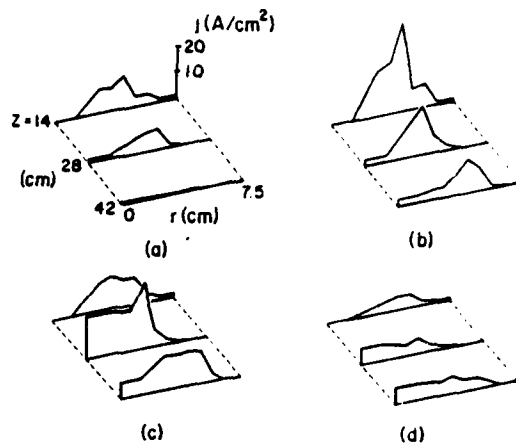
Fig. 6. Radial ion current density profiles. (a) 40 ns, (b) 60 ns, (c) 80 ns (d) 100 ns after initiation of diode voltage.

files at three different axial locations are shown in Fig 6. Note that the beam moves inward about 70 ns after the onset of the diode voltage pulse. The delay is due in part to the ion transit time through the drift tube and also to delays in the onset of electron neutralization of the beam space charge.

The signals from the iron and brass aperture Faraday cups can be combined to estimate the beam potential and the degree of neutralization in the beam. The difference between the signals is the electron current density. Assuming that the ion and electron charge densities are nearly equal, we estimate the velocity of the co-drifting electrons from

$$v_e = \left(\frac{J_{ion} - J_{net}}{J_{ion}} \right) v_{ion} \qquad (1)$$

The ion velocity is determined from the diode voltage. Since the electrons are emitted from the cathode at ground potential, their velocity provides a measure of the local potential inside the beam.

$$V_{space} = \frac{m \, v_e^2}{2 \, e} \qquad (2)$$

Fig. 7. Beam potential at 3 cm radius, 27 cm from cathode. The time scale is not referenced to the beam pulse.

Figure 7 shows an example of the potential, calculated in this manner, at a 3 cm radius, 27 cm from the diode. The space potential varies radially 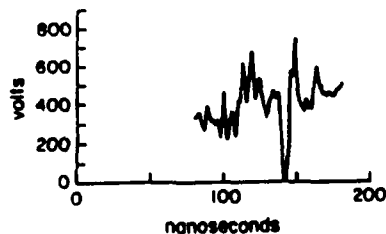and on a shot to shot basis. Values up to a factor of three larger than that shown in the figure have been recorded. The electron drift velocity calculated using Eq. 1 gives a velocity approximately equal to or slightly larger than the ion drift velocity. This result is within the range expected on the basis of the one dimensional theory of space charge neutralization. Finally, we use the space potential to check on the assumption of equal ion and electron densities. A characteristic solution of Poisson's equation shows the charge imbalance to be of order of 0.02%, and in accordance with the assumptions made in deriving the space potential.

Post Acceleration

Beam propagation has been measured across the second gap using carbon activation.

At currents above 1.5 kA, the protons in the beam will slow down upon entry into the gap, increasing the local charge density. In order to minimize the divergence caused by space charge in the gap the beam current was decreased below this value. The propagation was measured by four targets just upstream of the second gap. The beam fluence upstream could then be calculated by scaling of the proton fluence incident on these targets; the downstream intensity was measured over the entire beam area. The carbon targets were placed in an annular pattern so that the radial profile of the beam could be measured in addition to the total transport. Beam fluence profiles upstream and downstream of the second gap are shown in Fig. 8. Propagation efficiency was measured at 88% for a 1500 A shot and 100% for an 800 A shot. The standard deviation error was 5%.

We have also used the radial profiles to obtain an estimate of the beam divergence in propagation through the second gap. We consider those protons incident at the gap between radii of 3.4 and 4.7 cm and calculate the fraction of those protons which finish downstream of the gap in the radial interval between 4.7 and 6.0 cm. The gap width is 3.8 cm. We find 56% and 31% of the protons, corresponding to the 1500 and 800 Ampere beams respectively, make this transition. For comparison, we note that unneutralized and
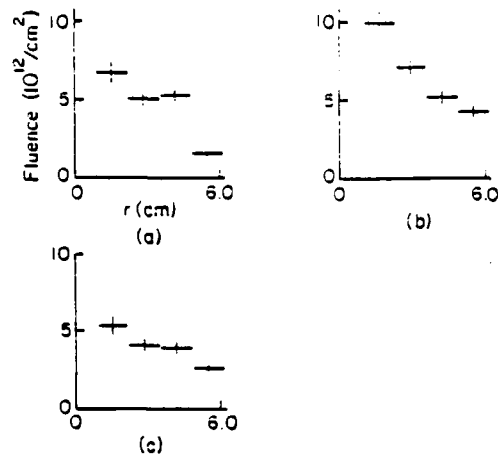
Fig. 8. Beam fluence (a) upstream of the second gap; (b) downstream of the second gap (1500 A); (c) downstream of the second gap (800 A).

unconfined beams of the same diameter and carrying the same currents as those reported above would have 50% and 31% of the protons make the radial transition.

Conclusions

We have developed and used an array of diagnostic techniques to study beam transport and neutralization along a uniform, strong axial magnetic field. The same techniques have been used to study beam transport through a 350 kV post acceleration gap. The beam dynamics observed approximate those expected on the basis of single particle orbits in the field geometry employed. An additional beam divergence is identified with the delay associated with space charge neutralization of the beam channel. Very efficient beam transport has been observed through the post acceleration diode. The beam divergence in that section of channel will require additional focussing in the gap, probably through field contouring.

References

1. S. Humphries, Jr., J. R. Freeman, J. Greenly, G. W. Kuswa, C. W. Mendel, J. W. Poukey, and M. Woodall. J. Appl. Phys. 41 (4), 1876 (1980).

2. I. S. Roth, J. D. Ivers, and J. A. Nation. Appl. Phys. Lett. 46 (3), 251 (1985).

3. T. Tanabe, A. Kana, K. Takahashi, A. Tokuchi, K. Masagata, M. Ito, and K. Yatsui. Phys. Rev. Lett. 56 (8), 831 (1986).

PROPAGATION OF INTENSE ION BEAMS IN IONIZED MEDIA

R. N. Sudan

Laboratory of Plasma Studies, Cornell University, Ithaca, NY 14853 USA

Abstract

The propagation of intense ion beams in an ionized medium and z-pinch current channels is examined. The analysis of beam dynamics includes both the induced return current and the self-consistent nonlinear response of the plasma ions. Stable propagation in channels is possible for regimes of interest to inertial fusion.

Introduction

An understanding of intense ion beam propagation is particularly important for inertial fusion reactor studies, and for injection of ion beams into magnetic traps for magnetic fusion. It may also have some relevance to the propagation of plasmoids in the solar atmosphere resulting from solar flares, to cometary tails, and possibly to such astrophysical phenomena as jets. This paper addresses the propagation of intense ion beams in (i) an ambient ionized medium and (ii) in preformed z-pinched current channels on a long enough time scale to include the motion of the background plasma ions. A brief discussion of the expected major instabilities is also undertaken.

Early experiments [1] confirmed that intense ion beams propagated freely in vacuum, provided electron emitting surfaces were available nearby for the almost complete space charge and current neutralization that is necessary. An elementary one-dimensional calculation [2] accounts for electron acceleration from such a surface by a potential $\phi_o = 2m_e v_o^2/e$ that develops across a narrow sheath; v_o is the beam velocity, and e and m_e are the electron charge and mass, respectively. C.G.S. electrostatic units will be used throughout. The accelerated electrons eventually thermalize through collective interactions [3,4] such that they acquire a thermal velocity v_o over and above their mean velocity v_o with a mean beam potential $e\bar{\phi} = 1/2\, m_e v_o^2$.

When a charge neutralized non-relativistic intense ion beam is injected across a static magnetic field $B\hat{z}$ in vacuum, it may propagate only if a polarizing electric field $E_y = v_o B/c$ can be maintained across the beam thickness by virtue of the y displacement of the accompanying electrons. This is possible if

$$4\pi n_b m_b v_o^2 /B^2 \ll 1 \qquad (1a)$$

$$(4\pi n_b m_b c^2/B^2)\,(a/\rho) \gg 1 \qquad (1b)$$

are satisfied [5,6]; $n_b m_b$ is the mass density of the beam, a is the half thickness and $\rho = m_b v_o c/eB_o$ is the beam ion Larmor radius. The subscript b refers to beam quantities throughout. When E_y is shorted out in a time less than the pulse duration τ either by the magnetic geometry or background plasma, then propagation ceases. For a weak magnetic field $B^2 < 4\pi\, n_b m_b v_o^2$ a current sheath may develop at the beam surface to exclude the external field. The actual details of the propagation for both cases require a study of the evolution of the space charge and current sheaths [7]. However, an application of the virial theorem to the beam propagating in vacuum is instructive and yields the global equation of motion [6]:

$$\frac{d}{dt}\int d^3x\; n_b m_b \mathbf{v}\cdot\mathbf{x}_\perp = \frac{1}{c}\int d^3x\; \mathbf{x}_\perp\cdot \mathbf{J}\times\mathbf{B} + \int d^3x P, \qquad (2)$$

with $P = n_b m_b v_\perp^2 + 3p_b + [(\delta E)^2 + (\delta B)^2]/4\pi$, p_b and $\mathbf{J} = \mathbf{J}_b + \mathbf{J}_e$ are the beam pressure and net current density respectively, $\mathbf{j}_e = -n e\, \mathbf{v}_e$ is the electron current density, δE and δB are the self-fields. Note that $n_e \approx n_b$ and $\mathbf{J}_b + \mathbf{J}_e \approx 0$ over the bulk of the beam except in the sheaths, so that the first term on the RHS of (2) is almost zero. Thus it is clear from (2) that the beam must expand in a vacuum magnetic field regardless of initial conditions.

In what follows we treat the injection and propagation of ion beams into a pre-ionized plasma.

Beam Driven Return Current

The injection of a beam of charged particles into a plasma is accompanied by a return current driven by the inductive electric field at the beam head [8]. This current decays [9] on a time scale $T = \pi\sigma a^2/c^2$ where σ is the conductivity, and a is the beam radius. However if the beam is diverging or converging, the beam radius, and

consequently the beam inductance, also varies, leading to a source of inductive voltage that can drive or decelerate the return current. In the early stages, or equivalently for short distances behind the beam head, we may neglect the motion of the background plasma ions. From Ampere's and Faraday's laws and employing Ohm's law $j_z = \sigma E_z = -(\sigma/c)\, \partial A/\partial t$, we obtain [10],

$$\frac{\partial A}{\partial t} - \frac{c^2}{4\pi\sigma} \frac{1}{r} \frac{\partial}{\partial r} r \frac{\partial A}{\partial r} = \frac{c}{\sigma} j_b(r,\, t - z/v_o), \quad (3)$$

where the magnetic field $B = \nabla \times A\, \hat{z}$. Let the injected beam profile be given by:
$j_b = \hat{z}\, [I_b/\pi a^2(t)]\, \exp{-(r^2/a^2)}\, U\,(t - z/v_o)$ and $U(x)$ is the unit step function. Solving (3) by standard techniques we obtain:

$$j_z = -\{J(t_*) +$$

$$\int_o^t dt_o\, (\dot{a}/a)\, \frac{2(r^2/a^2)}{(1+\tau/T)}\, J(\tau)\, U(t_o - z/v_o)\} \quad (4a)$$

$$\equiv j_I + j_{II}$$

with $t_* = z/v_o$, $\dot{a} = da/dt_o$, $\tau = t - t_o$, $T = \pi\sigma^2/c^2$,

$$J(a(t_o), t - t_o) = \frac{I_b\, \exp\{-r^2/a^2(t_o)[1+\tau/T]\}}{\pi a^2(t_o)(1 + \tau/T)}, \quad (4b)$$

and $J(t_*) \equiv J(a(t_*),\, t - t_*)$.

The first term j_I of (4a) is the usual response obtained when the beam radial profile is constant, i.e., $\dot{a} = 0$. The second term j_{II} depends on $\dot{a}$. For an expanding beam with $\dot{a} > 0$ this component has the sign of j_I but for $\dot{a} < 0$, i.e., a converging beam, it opposes j_I. Thus in a converging beam the net return current is diminished leading to increased focusing by the self-magnetic field. The radial distribution of j_{II} is different from j_I; j_{II} peaks near the beam edge since it is driven by beam expansion/contraction. In the limit $\tau \ll T$ we find,

$$j_{II} = -(I_b/\pi r^2)\, x$$

$$\{\Gamma(2,\, r^2/u^2 t^2) - \Gamma(2,\, r^2 v_o^2/z^2 u^2)\}, \quad (5)$$

where $\Gamma(p,\zeta) = \int_\zeta^\infty dt\, t^{p-1} \exp(-t)$ is the incomplete gamma function and $u \equiv \dot{a}$ is taken as

constant. The magnetic field is given by
$$B_\theta = -\partial A/\partial r = r^{-1} \int_o^r dr\, r\, (j_b + j_I + j_{II}).$$

Beam Dynamics

The momentum conservation equation for an axi-symmetric beam ($\partial/\partial\theta = 0 = \partial/\partial z$) with transverse pressure P, density n_b and radial velocity u is expressed as:

$$\frac{\partial}{\partial t}(n_b m_b u) + \frac{1}{r}\frac{\partial}{\partial r}(r n_b m_b u) = -\frac{\partial P}{\partial r} - \frac{1}{c} j_b B_\theta. \quad (6)$$

Integrating this equation over $r\, dr$ from 0 to ∞ and recognizing that the number of beam particles per unit length $N_b = 2\pi \int_o^\infty dr\, r\, n_b$ is conserved we obtain,

$$N_b m_b \frac{d}{dt} \bar{u} = 2\pi \int_o^\infty dr\, P - 2c^{-2} \int_o^\infty dr\, I_b \frac{dI}{r dr}, \quad (7)$$

with $N_b \bar{u} = \int_o^\infty dr\, r\, n_b u$, $I_b = 2\pi \int_o^r dr\, r\, j_b$ and the net current $I = 2\pi \int_o^r dr\, r\, (j_b + j_p)$; j_p is the induced plasma return current. Let the pressure $P = n_b m_b v_o^2 (\Delta\theta)^2$, where $\Delta\theta$, the beam divergence, varies adiabatically with exponent $\gamma = 2$, so that

$$(\Delta\theta)^2 = (\Delta\theta)_o^2\, a_o^2/a^2. \quad (8)$$

The radial scale length or beam radius is a. Recognizing that the flux $\propto \int_o^\infty dr\, B_\theta$ is conserved, (7) may now be written as,

$$N_b m_b \ddot{a} = 2N_b T_o a_o^2/a^3 - fI_b^2/c^2 a, \quad (9)$$

where $\dot{a} = \bar{u}$, $I = fI_b$, f is the fractional current neutralization of the beam, $fI_b^2/a = \int drfI_b^2/r$ and $T_o = m_b v_o^2(\Delta\theta)_o^2$. At equilibrium $\ddot{a} = 0$, and with no neutralization (f=1) we obtain the Bennett pinch condition $I_b^2 = 2N_b T_o$. On the contrary at injection, $f \ll 1$ and the Bennett pinch condition is not satisfied. Choosing a=0 at t=0 and f=0, (9) furnishes the solution

$$a(t)/a_o = (1 + t^2/t_b^2)^{1/2} \quad (10)$$

with $t_b = a_o/\sqrt{2}\, v_\theta(\Delta\theta)_o$. If $f \neq 0$ the first integral of (9) is given by:

$$\frac{1}{2}\bar{u}^2 \equiv \frac{1}{2}(\dot{a})^2 = (T_o/m_b)(1 - a_o^2/a^2) -$$

$$(\Pi_b^2/N_b m_b c^2)\, \ln a/a_o. \qquad (11)$$

The radius at which the self-pinching force finally catches up with the pressure term, i.e., where $\dot{a} = 0$ is

$$a_f \approx a_o \left\{ \exp N_b T_o c^2/\Pi_b^2 \right\} \equiv a_o \exp n. \qquad (12)$$

The beam expands to radius a_f in a time $t_b \approx (\pi/2)^{1/2} a_o e^n [\Pi_b^2/N_b m_b c^2]^{1/2} \phi(n)$, where ϕ is the error integral. If t_b is much less than T we are justified in treating $f \propto t/T$ as slowly varying in (9). If the final radius is not to be excessively large compared to the injection radius a_o, it is imperative to reduce the initial divergence $(\Delta\theta)_o$ and increase f by reducing the resistive decay time T by injection into an initially un-ionized medium.

If the beam is injected into a highly resistive medium such that initially, the magnetic force exceeds the pressure force, the final self-pinched radius a_f is less than a_o and is given by

$$(a_f/a_o)\ln(a_o/a_f) = N_b T_o c^2/\Pi_b^2. \qquad (12a)$$

Finally one might argue that since eventually all the return current will decay for a long enough beam $L > v_o T$, $f \to 1$ and the tail end of the beam will eventually self-pinch. In this situation, one has to consider other competing processes such as kink instabilities, etc.

Plasma Response to Beam Expansion

So far in determining the return current j_p and its influence on beam dynamics through the current neutralization factor f we have ignored the response of the background plasma ions. In the same geometry of the previous sections we now include the plasma response in the pressureless fluid approximation. Thus with $n_b \ll n$, the plasma ion density,

$$j_z = \sigma\left(E_z + \frac{1}{c}v_r B_\theta\right) = -\frac{\sigma}{c}\left(\frac{\partial A}{\partial t} + v_r\frac{\partial A}{\partial r}\right)$$

$$\equiv -\frac{\sigma}{c}\frac{dA}{dt}, \qquad (13)$$

$$-\frac{c}{4\pi r}\frac{\partial}{\partial r} r\frac{\partial A}{\partial r} = fj_b + j_z = fj_b(r,t) - \frac{\sigma}{c}\frac{dA}{dt}, \qquad (14)$$

$$nm\frac{d}{dt}v_r = -\frac{1}{c}j_p B_\theta = \left(\frac{\sigma}{c}\frac{dA}{dt} + (1-f)j_b\right)\frac{1}{c}\frac{\partial A}{\partial r}, \qquad (15)$$

$$\frac{\partial n}{\partial t} + \frac{1}{r}\frac{\partial}{\partial r} rnv_r = 0. \qquad (16)$$

We have three equations (12), (13), and (14) to determine the vector potential A, the plasma density n and the plasma ion radial velocity v_r, given $j_b(r,t) = n_b(r,t)\, ev_o$, the beam current density profile.

Infinite Plasma Conductivity $\sigma \to \infty$

This is a particularly simple case for which we derive an exact nonlinear solution of the form where the driving beam current profile is $j_b(r,t) = j_b(r')$ with $r' = (r^2 - 2\alpha t)^{1/2}$ with α a constant. In other words we regard the beam to expand in such a manner that the local Lagrangian beam particle velocity $dr/dt = -\alpha/r$. All quantities n, v_r and A depend only on r' then since $\sigma \to \infty$ and j_z must be finite, from (13),

$$\frac{dA}{dt} = 0 = \left(-\frac{\alpha}{r} + v_r\right)\frac{\partial A}{\partial r}. \qquad (17)$$

Note that $\partial A/\partial t = -(\alpha/r')\partial A/\partial r'$ and $\partial A/\partial r = (r/r')\partial A/\partial r'$. The conclusion from (17) is that either $\partial A/\partial r = 0$ or $v_r = \alpha/r$. If $\partial A/\partial r = 0$ then $B_\theta = 0$

$$j_z + fj_b = 0, \qquad (18)$$

i.e., current neutralization is perfect and is maintained as the beam expands. This is not a surprising conclusion for $\sigma \to \infty$. Indeed if (18) holds the beam may expand in any arbitrary fashion. On the other hand if $v_r = \alpha/r$ then the continuity equation (16) is satisfied for arbitrary density profile $n(r')$. Furthermore, dv_r/dt also vanishes and hence because $B_\theta \neq 0$

$$j_z(r') = 0, \qquad (19a)$$

i.e., there is no return current. From (14) with $B_\theta(r') = (r'/r)B_\theta(r)$, we obtain,

$$rB_\theta(r,t) = rB_\theta(r,0) + \frac{4\pi}{c}\int_r^R dr'\, r_b'\, f\, j_b(r'), \qquad (19b)$$

where $R = (r^2 + 2\alpha t)^{1/2}$. In this solution the plasma move radially outward with $v_r = \alpha/r$ and the electric field vanishes in the frame moving with this velocity and hence $j_z(r') = 0$.

Finite Conductivity

We now treat the more important case of finite conductivity. In order to simplify the analysis of (13) to (16) we proceed to the limiting case of slab geometry where $r = R + x$ with $x \ll R$. In this limit (13) to (16) become

$$j_z = -(\sigma/c)(\partial A/\partial t + v_r \partial A/\partial x), \qquad (20)$$

$$\frac{\partial^2 A}{\partial x^2} = -\frac{4\pi}{c}(fj_b + j_z), \qquad (21)$$

$$nm(\frac{\partial}{\partial t} v_r + \frac{\partial}{\partial x} v_r) = -\frac{\partial A}{\partial x}\{j_b + \frac{c}{4\pi}\frac{\partial^2 A}{\partial x^2}\}, \qquad (22)$$

$$\frac{\partial n}{\partial t} + \frac{\partial}{\partial x} nv_r = 0. \qquad (23)$$

Let $fj_b(x,t) = fj_b(x')$ with $x' = x-ut$, u constant and n, A, and v_r have the same functional dependence. From (20), (22), and (23) we obtain,

$$j_z = (\sigma/c)(u-v_r)\partial A/\partial x', \qquad (24)$$

$$n(u - v_r) = n_o u, \qquad (25)$$

$$v_r = (8\pi n_o mu)^{-1}\{(\partial A/\partial x')^2 + 2\int_{x'}^{\infty} dx\, j_b dA/dx\}, \qquad (26)$$

with $\partial A/\partial x' = 0 = v_r$ at $x' = \infty$. Subtracting these expressions in (21) we obtain

$$\frac{db}{d\chi} = b(b^2 - 1) + fJ_b + 2b\int_{\chi}^{\infty} dx'\, J_b b, \qquad (27)$$

where $b^2 = B_\theta^2/\pi n_o mu^2$, $B_\theta = -dA/dx'$, $\chi = x'/\delta$, $\delta = c^2/4\pi\sigma u$ and $J_b = j_b(c/\sigma u)(8\pi n_o mu^2)^{-1/2}$. In the region outside the beam where $J_b = 0$, (27) has the solution

$$b(\frac{1-b}{1+b})^{1/2} = b_o(\frac{1-b_o}{1+b_o})^{1/2} \exp{-\chi} \qquad (28)$$

where $b = b_o$ at $\chi = 0$ or $x' = R$ and $b < 1$ everywhere. Furthermore, no solutions exist with acceptable boundary conditions for $b_o^2 \geq 1$. Indeed if $b_o \geq 1$ then the density $n = n_o/(1-b^2)$ will become infinite at some finite χ, i.e., the laminar solution ceases to exist because the fluid particles are suffering a reflection at this point by virtue of the strong magnetic field.

Let fj_b the net beam current be located in a thin shell of radius a and small thickness $\Delta \ll a$. In this case the solution within the beam is approximately $b = 0$ and $B_o = 4\pi fj_b\Delta/c$. Then the conclusion from the above considerations is that for

$$B_o < (8\pi n_o mu^2)^{1/2}, \qquad (29)$$

as the beam expands with velocity $\dot{a} = u$ a laminar disturbance is set up in the surrounding plasma that typically extends for a distance $c^2/4\pi\sigma u$ beyond the expanding beam. If fj_b increases to a value such that $B_o = \sqrt{8\pi n_o mu^2}$ then the disturbance cannot be laminar and the fluid is reflected by the magnetic field of the expanding beam. If this situation obtains then the rate of momentum gain by the plasma ions $2\pi an_o m(\dot{a})^2$ has to be balanced by the magnetic pressure force $(B_o^2/8\pi)2\pi a$, i.e., $B_o^2 = 8\pi n_o mu^2$, which is precisely the condition (29) derived above. Soon after injection B_o is small and u is large so that (29) is satisfied and a laminar disturbance propagates through the plasma. As B_o increases with f and $\dot{a}$ decreases with time, ultimately (29) is violated. During this last phase, the magnetic pressure term in (9) should be replaced by $2\pi an_o m(\dot{a})^2$. If by this stage the pressure term is negligible then,

$$\dot{a} = u_o \exp{-(a^2-a^2)/a_*^2}, \qquad (30)$$

where $a_*^2 = N_b m_b/\pi n_o m$ and $u_o = \dot{a}$ at $a = a_o$.

Propagation In Ionized Current Channels

One of the critical issues in Light Ion Inertial Fusion (LIIF) schemes is the transport of multi-megampere, multi-megavolt light ion beams over distances 2-5 m to the target pellet from the injection port. One promising possibility involves the use of preformed z-pinch plasma column channels to guide the beam to target [11]. After such a channel is formed by one of several techniques, the azimuthal magnetic field B_θ confines the beam ions radially. Space charge and current neutralization are provided by the high plasma density in the channel $(n > 10^{17} cm^{-3})$. The propagation of beam ions in such channels has been studied (i) using one dimensional r-dependent models [11,12] and (ii) two dimensional (r-z) models employing a hybrid 2-1/2 developed simulation code CIDER developed at Cornell University [13]. These 2-d simulations show that 5-7 MeV, 1-2 MA proton beams with initial divergence $\Delta\theta$ of order a few degrees propagate with an energy efficiency of ~70 % in a

4 m ionized hydrogen channel of density $\sim 10^{18}$ cm^{-3} without revealing any gross axisymmetric instabilities. The energy loss results from: (i) the direct collisions between the beam ions and the plasma ions and electrons and (ii) the Ohmic losses suffered by the return current [10].

We will consider here the dynamics of beam propagation in such channels. Prior to the injection of the beam into the channel it is assumed that an equilibrium exists between the magnetic and pressure forces, i.e.,

$$\frac{\partial p}{\partial r} = - \frac{B_\theta}{4\pi r} \frac{\partial}{\partial r} r B_\theta, \tag{31}$$

and $I_c = \pi a^2 j_c$ is the channel z-current. Furthermore, the beam must be injected before any gross instability of the channel, viz. the kink, sets in on a time scale $t_k = \gamma^{-1}$ where $\gamma \sim [B_o/(4\pi m)^{1/2}]k \ln(1/ka)$; $B_o = 2\pi j_c a/c$, a is the channel radius, $k = 2\pi/\lambda$ and γ is the kink wavelength. The injected beam is expected to satisfy the equilibrium relation

$$\frac{\partial P}{\partial r} = - \frac{1}{c} j_b B_\theta + n_b e E_r, \tag{32}$$

where E_r is the Hall radial field required to set up the return current, and $P = n_b m_b v_o^2 (\Delta\theta)^2$. If the injected beam does not satisfy (32) then it may either expand or contract until it settles to an equilibrium radius determined by an equation similar to (12) with TI_b^2 replaced by $I_b B_o a/2$. The channel plasma dynamics is governed by:

$$nm \frac{d v}{d t} = -\nabla p + \frac{1}{c} j_c \times B + \frac{1}{c} j_p \times B - n_b e E, \tag{33}$$

$$j_p = \sigma(E + \frac{1}{c} v \times B - j_p \times B /n_e ec), \tag{34}$$

$$c\nabla \times B = 4\pi(j_c + j_b + j_p), \tag{35}$$

$$n_e = n_i + n_b. \tag{36}$$

Immediately after beam injection the induced plasma current $j_p = - j_b = -n_b e v_o \hat{z}$. From the r-component of (34) and $j_{pr} = 0$ we obtain the Hall electric field $E_r = (n_b/n_e) v_o B_\theta/c$. Thus for $n_b \ll n_e$, E_r may be neglected in (33). Integrating (33) over rdr and using the continuity equation we obtain

$$Nm \frac{d}{dt} \bar{v}_r \equiv Nm \, \dot{a} = \frac{1}{c} \int_0^a dr \, j_b B_\theta r. \tag{37}$$

For high enough channel conductivity the flux $\psi = \int dr B_\theta$ is conserved during the expansion of channel. Thus

$$\dot{a} = K/a ; \quad K = (I_b/3I_c)(B_o^2/4\pi nm). \tag{38}$$

The solution of (38) is given by,

$$\dot{a} = \{2K[\ln a/a_o]\}^{1/2}, \tag{39}$$

$$(a/a_o) F[(\ln a/a_o)^{1/2}] = (K/2a_o^2) t, \tag{40}$$

where $F(x) = \exp(-x^2) \int_0^x dy \exp(y^2)$. For $a = a_o + \delta a$, $\delta a < a_o$ we obtain

$$\delta a/a_o = t^2/t_c^2 ; \tag{41a}$$

$$t_c = (3I_c /I_b^{1/2})a_o/v_A, \quad v_A^2 = B_o^2/4\pi n_o m. \tag{41b}$$

Now since the beam ion betatron time $t_\beta = a_o/v_o\Delta\theta \ll t_c$, the beam contained by the channel magnetic field expands adiabatically with the channel radius but satisfying (32). From (40) for $a/a_o = 2$, $t/t_c = 0.9$ and for $a/a_o \gg 1$ the beam and channel expand almost linearly with time. If the beam expansion is to be limited during propagation the beam pulse width $\tau < \tau_c$. The channel expansion may ultimately be solved by the dense neutral gas surrounding the channel that absorbs the momentum through ion neutral collisions provided $\nu_{in} t_c \geq 1$; ν_{in} is the ion neutral collision frequency.

Kink Instability

After a time t_c the return current decays a little and the net beam current $I = fI_b$ ($f = t_c/T$, $T = \pi\sigma a^2/c^2$) increases the magnitude of the magnetic field causing the beam to pinch. This could lead to non-axisymmetric instabilities not covered by previous 1-d and 2-d simulation studies [11,12,13]. Since the resistive hose grows on the time scale T and the pulse width $\tau \ll T$, we need not be concerned with this particular instability. On the other hand, the kink instability occurs also in the infinite conductivity limit and we must, therefore, examine this case next.

For the purpose of this calculation, we shall assume that either the channel has stopped expanding or that the expansion rate is much slower than the growth rate γ if any, of the kink instability, i.e., $\gamma > \dot{a}/a \sim t_c^{-1}$. Let the plasma displacement be described by $\xi \sim \exp i(kz+\theta-\omega t)$.

Then from the perturbed mhd equation for plasma motion we obtain

$$-\omega^2 \int d^3x\, n m \left|\xi\right|^2 = -e\int(n_b\xi^* \cdot \delta E + \delta n_b\, \xi^* \cdot E\,)d^3x -$$

$$\int d^3x\, \xi \cdot \nabla\delta p + \frac{1}{c}\int d^3x\, \xi^* \cdot j_p \times \delta B +$$

$$\frac{1}{4\pi}\int d^3x\, \xi^* \cdot (\nabla \times \delta B)\times B - \frac{1}{c}\int d^3x\, \xi^* \cdot \delta\, j_b \times B \ . \tag{42}$$

Now with δf respresenting the perturbed beam distribution we write,

$$I_1 \equiv -\frac{1}{c}\int d^3x\, \xi^* \cdot \delta\, j_b \times B \ -e\int d^3x\, \delta n_b\, \xi^* \cdot E$$

$$= -e\int d^3x\, d^3v\, \xi^* \cdot (\, E + \frac{1}{c}V\times B\,)\delta f$$

$$= -m_b\int d^3x\, d^3v(\, \xi^* \cdot \frac{d\,v}{d\,t})\delta f$$

$$= m_b\int d^3x\, d^3v\{(\, \xi^* \cdot v\,)\frac{d}{dt}\delta f + (\, v \cdot \frac{d}{dt}\xi^*\,)\delta f\},$$

(by virtue of Liouvilles' theorem)

$$= \int d^3x\, d^3v\{e(\, \xi^* \cdot v\,)(\, \delta E + \frac{1}{c}v\times\delta B\,)\cdot\frac{\partial f}{\partial v}$$

$$+ m_b(\, v \cdot \frac{d}{dt}\, \xi^*\,)\delta f\},$$

(employing Vlasov equation)

$$= e\int d^3x\, d^3v(n_b\xi^* \cdot \delta E + \xi^* \cdot j_b\times\delta B\,) +$$

$$m_b\int d^3x\, \delta f(\, v \cdot \frac{d}{dt}\, \xi^*\,).$$

Employing the above expression in [42] we obtain [14]

$$\omega^2\int d^3x\, n m \left|\xi\right|^2 = -\int d^3x\, \delta p(\nabla \cdot \xi^*)$$

$$-\frac{1}{c}\int d^3x\, \xi^* \cdot (\, j_p + j_b)\times \delta B$$

$$+\frac{1}{4\pi}\int d^3x\, \left|\delta B\right|^2 + m_b\int d^3x\, d^3v\delta f(\, v \cdot \frac{d}{dt}\, \xi^*). \tag{43}$$

For the kink stability we set $\nabla \cdot \xi^* = 0$ thereby annihilating the first term on the RHS of (43). The last term of the RHS can be computed by solving for δf from the Vlasov equation:

$$\delta f = \frac{e}{m_b}\{\delta A\frac{\partial f}{\partial v_z} - i(\omega\frac{\partial f}{\partial\epsilon} +$$

$$k\frac{\partial f}{\partial v_z})\int_{-\infty}^{t} dt'\, v_z\delta A_z\}. \tag{44}$$

(Where $\delta A_z = \xi B_\theta$, $\xi = \xi\,(\hat r + i\hat\theta)\, \exp i$
$(kz + \theta - \omega t)$, $\epsilon = v^2/2$, ξ is constant.)
Substituting δf in I_2 and employing betatron motion of the beam ions to evaluate the time history integral we obtain,

$$I_2 \equiv m_b\int d^3x\, d^2v\delta f\, v \cdot (-i\omega + v \cdot \nabla)\, \xi^*$$

$$= \left|\xi\right|^2\ \frac{I_b B_*(kv_o-\omega)^2}{(kv_o-\omega)^2 - \omega_\beta^2}\ .$$

In arriving at this expression we have chosen the beam distribution $f \sim \exp-(m_b/T_b)(\epsilon - v_o v_z)$ and $B_\theta = B_* r/a$ is determined by the net current density $= j_p + j_b = \hat z(j_c + f j_b)$, where $f \sim t_c/T$. The betatron frequency of the beam ions is $\omega_\beta = (eB_* v_o/m_b ac)^{1/2}$. The remaining terms of (43) represent the mhd contribution from a [15] channel carrying the net current $I_c + f I_b$ and can be treated in the conventional manner. Finally we obtain:

$$\omega^2 = \frac{B_*^2}{4\pi n m a^2}\{-k^2a^2\ln\frac{1}{ka} + (\frac{I_b}{I_c+fI_b})\frac{(kv_o-\omega^2)}{(kv_o-\omega^2)-\omega^2\beta}\}, \tag{45}$$

where $B_* = 2(I_c+fI_b)/ac$. The beam term is stabilizing for perturbations with wavelengths satisfying the inequality [16]

$$k^2 > \omega_\beta^2/v_o^2 \equiv k_\beta^2. \tag{46}$$

For stable propagation we also require

$$k^2a^2\ln(1/ka) < I_b/(I_c + fI_b). \tag{47}$$

Identifying the longest unstable wavelength with the beam pulse length $L = v_o\tau$, stable propagation is achieved if

$$(2\pi a)^2(I_c+fI_b)/I_b < v_o^2\tau^2 < (2\pi v_o/\omega_\beta)^2. \tag{48}$$

This result is accompanied by a caveat. For unstable long pulse lengths the growth rate γ from (45) is approximately $\gamma\tau \sim 2\pi/\omega_\beta t_*$; t_* is obtained from (41) with $I_c + fI_b$ replacing I_c. The basic justification for the analysis that requires $\gamma t_{c*} > 1$ may not hold. However, the treatment of the stability of an expanding current column is nontrivial but it is unlikely that an exact treatment will lead to a more pessimistic picture because an expanding channel

reduces the free energy available for kinking. In any case, the number of e-folds $\gamma\tau \sim t_\beta/t_{c*}$ computed from the above analysis is less than unity in a dense channel.

Filamentation Instability

Although generally speaking the beam pulse time $\tau \ll T$ the return current resistive decay time, this may not be case for a filament of the beam of width $\Delta \ll a$ for which the decay time $T_\Delta \sim \pi\sigma\Delta^2/c^2$. The decay of the return current in the filament is accompanied by a magnetic field $B = 2\pi e n_b v_o (t/T_\Delta)^{1/2}\Delta/c$ at the filament surface. The filament will self-pinch via the filamentation instability [17,18], at say $t = \tau/2$ if

$$\eta = 8\pi P/B^2 = 4m_b(\Delta\theta)^2\sigma/n_b e^2\tau < 1. \qquad (49)$$

Note that η is independent of Δ and is identical to $NT_o c^2/I I_b^2$ of (12) for $f_\tau = \tau/2T$. If the beam satisfied [32] at injection then $(\Delta\theta)^2 \sim eB_o a/m_b c v_o$ and $\eta = 4\, I_c/f_\tau I_b$. If $\eta > 1$ the beam will propagate without filamentation. On the other hand if $\eta < 1$, filamentation will proceed until the beam divergence increases through nonlinear evolution such that the state $\eta = 1$ is reached. Thus the filamentation instability does not appear crucial to propagation in ionized current channels.

In conclusion it appears safe to predict that intense ion beams of suitably short duration may safely be propagated in straight, well formed current carrying channels of sufficient mass density. It is amusing to note that ultimately the confinement mechanism for the beam relies on channel plasma inertia.

Acknowledgements

References

1. S. Humphries, J.J. Lee, and R.N. Sudan, J. Appl. Phys. 46, 187 (1975).

2. S. Humphries, Appl. Phys. Lett. 32, 792 (1978).

3. S. Humphries, T.R. Lockner, J.W. Poukey, J.P. Quintenz, Phys. Rev. Lett. 46, 995 (1981).

4. R.N. Sudan, Appl. Phys. Lett. 44, 975 (1984).

5. W. Peter, A. Ron, and N. Rostoker, Phys. Fluids 22, 1471 (1979); W. Peter and N. Rostoker, Phys. Fluids 25, 730 (1982).

6. R.N. Sudan, "Propgation of Intense Pulsed Ion Beams", Laboratory of Plasma Studies Report 322, Cornell University, Ithaca, NY (1983).

7. W. Peter, A. Ron and N. Rostoker, Phys. Fluids 26, 2276 (1983).

8. D.A. Hammer and N. Rostoker, Phys. Fluids 13, 1831 (1970).

9. R. Lee and R.N. Sudan, Phys. Fluids 14, 1213 (1971).

10. R.V. Lovelace and R.N. Sudan, Phys. Rev. Lett. 27, 1256 (1971).

11. J.R. Freeman, L. Baker, and D.L. Cook, Nucl. Fusion 22, 383 (1982).

12. D.G. Colombant, S.A. Goldstein, and D. Mosher, Phys. Rev. Lett. 45, 1253 (1980).

13. A. Mankofsky and R.N. Sudan, Nucl. Fusion 24, 827 (1984).

14. R.N. Sudan and M.N. Rosenbluth, Phys. Rev. Lett. 36, 972 (1976); Phys. Fluids 22, 282 (1976); J.M. Finn and R.N. Sudan, Nucl. Fusion 22, 1443 (1982).

15. See for example, B.B. Kadomstev, Review of Plasma Physics, Vol. 2, Edit. M.A. Leontovich (Academic Press, New York, 1966) p. 165.

16. R.V. Lovelace, Phys. Rev. Lett. 35, 162 (1975); Phys. Fluids 19, 723 (1976).

17. R.F. Hubbard and D.A. Tidman, Phys. Rev. Lett. 41, 866 (1978).

18. E.P. Lee, S. Yu, H.L. Buchanan, F.W. Chambers, and M.N. Rosenbluth, Phys. Fluids 23, 2095 (1980).